

# Thermal and Catalytic Decomposition of 2-Hydroxyethylhydrazine and 2-Hydroxyethylhydrazinium Nitrate Ionic Liquid

Steven D. Chambreau, Denisia M. Popolan-Vaida, Oleg Kostko, Jae Kyoo Lee, Zhenpeng Zhou, Timothy A. Brown, Paul Jones, Kuanliang Shao, Jingsong Zhang, Ghanshyam L. Vaghjiani,\* Richard N. Zare, and Stephen R. Leone



Cite This: *J. Phys. Chem. A* 2022, 126, 373–394



Read Online

ACCESS |



Metrics & More

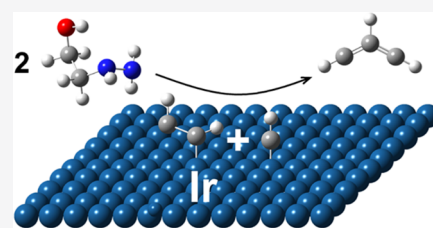


Article Recommendations



Supporting Information

**ABSTRACT:** To develop chemical kinetics models for the combustion of ionic liquid-based monopropellants, identification of the elementary steps in the thermal and catalytic decomposition of components such as 2-hydroxyethylhydrazinium nitrate (HEHN) is needed but is currently not well understood. The first decomposition step in protic ionic liquids such as HEHN is typically the proton transfer from the cation to the anion, resulting in the formation of 2-hydroxyethylhydrazine (HEH) and  $\text{HNO}_3$ . In the first part of this investigation, the high-temperature thermal decomposition of HEH is probed with flash pyrolysis ( $<1400$  K) and vacuum ultraviolet (10.45 eV) photoionization time-of-flight mass spectrometry (VUV-PI-TOFMS). Next, the investigation into the thermal and catalytic decomposition of HEHN includes two mass spectrometric techniques: (1) tunable VUV-PI-TOFMS (7.4–15 eV) and (2) ambient ionization mass spectrometry utilizing both plasma and laser ionization techniques whereby HEHN is introduced onto a heated inert or iridium catalytic surface and the products are probed. The products can be identified by their masses, their ionization energies, and their collision-induced fragmentation patterns. Formation of product species indicates that catalytic surface recombination is an important reaction process in the decomposition mechanism of HEHN. The products and their possible elementary reaction mechanisms are discussed.



## 1. INTRODUCTION

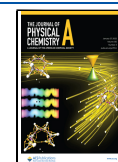
The application of energetic materials based on room-temperature ionic liquids (RTILs) continues to provide an important strategy to develop new monopropellants that can provide enhanced performance capabilities compared to the current state-of-the-art baseline system, which is hydrazine ( $\text{N}_2\text{H}_4$ ).<sup>1</sup> Furthermore, the strong Coulombic bonding present in these ionic materials imparts a very low vapor pressure.<sup>2</sup> Consequently, their handling does not require the precautions and safety protocols associated with the highly toxic hydrazine. However, reliable ignition and sustained combustion of these energetic materials present major challenges, as washout (flame quenching) can be a major concern.<sup>3</sup> Therefore, to fully utilize the available energy release of these RTIL monopropellants, the ignition and combustion behaviors of these materials need to be characterized. This information is required to construct detailed chemical ignition and combustion models that would facilitate the design and evaluation of the combustion chamber configuration for a given thruster application. To have reliable, sustained ignition in high-energy-density fuels, it is necessary to control the conditions that will lead to flammable gas mixtures and to avoid conditions and thruster geometries leading to instabilities in the flame that can cause washout. Ignition leading to sustained combustion occurs when a sufficient amount of heat is released into a gas mixture within the proper flammability limits.<sup>4</sup>

The substantially higher adiabatic flame temperatures of these fuels (typically  $>1800$  °C) and the corrosive nature of the combustion products (e.g.,  $\text{NO}_x$ , super-heated steam, and  $\text{CO}_2$ ) present a particular difficulty in high-temperature material design that can withstand the extreme thermochemical environment during ignition and combustion of these monopropellants.<sup>5</sup> While ignition is exclusively a gas-phase phenomenon that can be described by chemical kinetics and flammability limit models,<sup>4</sup> there are condensed-phase homogeneous and heterogeneous processes that produce the gaseous species that contribute to ignition.<sup>6–11</sup> Although many physical and thermodynamic properties of materials are now being predicted theoretically with reasonable reliability using molecular dynamics and quantum chemical ab initio computations,<sup>12,13</sup> the same is not true for a priori prediction of their chemical reactivity. This is because, often, detailed mechanistic information on the transient and dynamical behavior of the system is lacking. Therefore, an important goal of our research is to use sensitive and selective

Received: August 20, 2021

Revised: November 1, 2021

Published: January 11, 2022



experimental probes to understand at the molecular level the underlying chemistry involved under relevant extreme environments. Molecular-level studies of the interfacial reaction chemistry are key to the development and improvement of theoretical models for catalytic ignition.

Vacuum ultraviolet photoionization time-of-flight mass spectrometry (VUV-PI-TOFMS), nanotip ambient ionization mass spectrometry (NAIMS),<sup>14</sup> and laser desorption/ionization droplet delivery mass spectrometry (LDIDD-MS)<sup>15</sup> provide the necessary experimental sensitivity and are used in this effort to investigate the thermal and catalytic reaction mechanisms. This experimental data intends to serve to guide an ab initio quantum chemical effort, yielding accurate reaction energetics and rate coefficients for the proposed catalytic reactions. This information will feed into chemical kinetics/multiphysics models that will make ignition predictions possible in high-temperature catalytic systems. This capability will lead to improved design of propellant formulations and catalysts resulting in sustained combustion and reliable propulsive thrust that could lead to the extension of thruster lifetimes.

While  $N_2H_4$  is a single species fuel, high-energy-density ionic liquid monopropellants consist of both the fuel (cation) and oxidizer (anion) constituents also containing O and C atoms that can greatly complicate the ignition and combustion reaction mechanisms versus  $N_2H_4$ . The ignition mechanism of  $N_2H_4$  involves both catalytic decomposition of  $N_2H_4$  on iridium<sup>16,17</sup> and homo- and heterogeneous thermal decomposition of  $N_2H_4$  prior to ignition.<sup>18–20</sup> Recent studies have shown that in the catalysis of  $N_2H_4$  with iridium, the interaction of the nitrogen lone pair with the Ir initiates  $N_2H_4$  chemisorption and the formation of mixed nitrides on the Ir surface, which react further to lead to  $NH_3$  and  $H_2$  as final products.<sup>21</sup> These catalytic and thermolytic decomposition products can then directly compete with  $N_2H_4$  for reactive sites on the Ir. To the best of our knowledge, the identities of the initial complexed species for 2-hydroxyethylhydrazinium nitrate (HEHN) on iridium have not been determined previously. Thermal decomposition of HEHN has been studied by Chowdhury and Thynell using confined rapid thermolysis (CRT)<sup>22</sup> and more recently by Esparza and co-workers by thermogravimetric analysis (TGA) coupled with mass spectrometry and Fourier-transform infrared spectroscopy.<sup>20</sup> These studies have both shown that the primary step in the decomposition reaction is the proton transfer from the hydroxyethylhydrazinium ( $HEH^+$ ) cation to the nitrate anion to produce 2-hydroxyethylhydrazine (HEH) and  $HNO_3$ . Based on the evolution profiles of products such as  $NH_3$ ,  $H_2O$ ,  $N_2$ ,  $NO$ ,  $CO_2$ ,  $N_2O$ , and  $NO_2$ , coupled with kinetic modeling, the models indicate that the subsequent reactions are likely autocatalytic with  $HNO_3$ .<sup>20</sup> In the CRT work, the proposed reaction scheme included three reaction steps: the first two being proton transfer and a subsequent reaction of HEH with  $HNO_3$  produced in the first step, while the third step was a global reaction with fractional stoichiometric values. In the TGA work, a heterogeneous reaction pathway for the production of  $NH_3$  and ethanolamine was proposed. Both studies yielded effective decomposition rate parameters that could be useful for simple kinetic modeling of HEHN chemistry. Here, one objective is to identify elementary reaction steps not previously proposed in the initial thermal and catalytic decomposition mechanisms to develop an improved decomposition mechanism for HEHN.

To discuss and understand the chemical processes involved when HEH and HEHN are thermally and catalytically decomposed (the latter on iridium surfaces), the structure of this paper is broken down as follows: (1) the unimolecular thermal decomposition of HEH by flash pyrolysis is presented in Section 4.1, (2) the thermal and catalytic decomposition of liquid HEHN using an effusive source with VUV-PI-TOFMS is presented in Section 4.2, (3) the thermal and catalytic decomposition of aerosol beams of HEH and HEHN via VUV-PI-TOFMS is presented in Sections 4.3–4.5, (4) the catalytic decomposition of HEHN via NAIMS is presented in Section 4.6, and (5) the catalytic decomposition of HEHN via LDIDD-MS is presented in Section 4.7.

## 2. EXPERIMENTAL SECTION

Experimental techniques that are employed in this work are fixed wavelength vacuum ultraviolet (10.45 eV) photoionization time-of-flight mass spectrometry (VUV-PI-TOFMS),<sup>23–27</sup> tunable VUV-PI-TOFMS (7.4–15 eV),<sup>6,7,28–33</sup> nanotip ambient ionization mass spectrometry (NAIMS),<sup>14</sup> and laser desorption/ionization droplet delivery mass spectrometry (LDIDD-MS).<sup>15</sup>

**2.1. Flash Pyrolysis VUV-PI-TOFMS.** The flash pyrolysis source was based on the design of Chen and co-workers.<sup>23</sup> The pyrolysis experiments were conducted on an apparatus that was previously described.<sup>24–27</sup> 2-Hydroxyethylhydrazine (HEH) was obtained from James Robinson Ltd. (>98% purity) and was used without further purification. HEH was introduced by bubbling He ( $P = 1.5$  atm) through the liquid at elevated temperature to control the vapor pressure. The bubbler bath temperature for HEH was  $T = 60$  °C, the vapor pressure of HEH was estimated to be  $P_{\text{vap}} = 100$  mTorr, and the concentration for HEH was low enough to avoid secondary reactions of the HEH and decomposition products in the source. Similarly, ethanol was introduced in a separate experiment with the bubbler bath temperature at  $T = 0$  °C. Flash pyrolysis was achieved by expanding the gas mixture through a heated SiC nozzle (Carborundum, heated length 10 mm, 2 mm o.d., 1 mm i.d.). The nozzle was heated resistively with the electrical current being controlled by a Variac transformer. The nozzle temperature was monitored by a type-C (Omega) thermocouple attached to the outside of the nozzle that had previously been calibrated to the internal temperature of the nozzle. With a near-sonic velocity of the sample within the nozzle, the residence time in the heater has been estimated to be approximately 50  $\mu\text{s}$ .<sup>23,37</sup> After leaving the nozzle, products were cooled and isolated by supersonic expansion into vacuum where they proceeded through a skimmer to the photoionization region.

The parent molecules and products were ionized by 118.2 nm (10.45 eV) photons produced by frequency tripling the 354.7-nm output of a Nd:YAG laser in a Xe cell (20 Torr) and were subsequently detected by a linear time-of-flight mass spectrometer (R. M. Jordan Co.). The 118.2-nm radiation was focused by a  $MgF_2$  lens through a small aperture into the photoionization zone, while the fundamental 354.7-nm beam diverged in this region. This divergence and the aperture minimized multiphoton ionization (MPI) and the amount of scattered 354.7-nm radiation within the ionization region. The TOF traces were collected using a digital oscilloscope (Tektronix TDS3032) and averaged over 512 laser shots; they were then converted to mass spectra using the appropriate Jacobian transformation.

**2.2. Effusive Beam, Tunable VUV-PI-TOFMS.** The end station for the collection of mass spectra of positive ions produced by photoionization of the HEHN decomposition products from an effusive source, described previously,<sup>6</sup> at the Chemical Transformations tunable vacuum ultraviolet Beamline 9.0.2.3 of the Advanced Light Source (ALS) Synchrotron facility, is described briefly here. The present experimental IL effusive source setup is a modification of a setup used previously<sup>28–32</sup> and used successfully in ref 33. It uses a new, smaller effusive IL source that is mounted directly onto the repeller plate of the mass spectrometer ion optics; a pinhole in the repeller plate introduces the HEHN decomposition product vapor into the ionization region. This new configuration increases the IL product vapor number density in the ionization region by approximately 250 times versus the previous setup. The IL effusive source was maintained between 373 and 473 K, initially with only the pure IL, and subsequently with the IL and a small amount of Ir catalyst has been added to the glass sample holder in order to compare thermal decomposition versus catalytic decomposition products. The HEHN sample (generated in-house at AFRL, purity >98%, GC/MS) was loaded into the source, mounted into the vacuum chamber, pumped to  $<10^{-7}$  Torr, and degassed for 12 h at 298 K, prior to carrying out the pure IL photoionization measurements. After the pure IL experiment, the vacuum chamber was vented, a new sample of HEHN and an Ir catalyst granule were introduced into the glass sample container, and the vacuum chamber was again pumped down to  $<10^{-7}$  Torr and degassed for 4 h at 298 K. The pressure in the interaction vacuum chamber during operation does not exceed  $1 \times 10^{-7}$  Torr ( $1.33 \times 10^{-5}$  Pa). Thermal decomposition of HEHN using thermogravimetric analysis (TGA) indicates that a 10% mass loss is achieved at 423 K at a heating rate of 1 K/min.<sup>20</sup> Here, it is assumed that HEHN has a negligible thermal decomposition at 373 K and a significant thermal decomposition at 473 K for this experiment.

The mass spectra and ion yields were measured with a pulsed TOF mass spectrometer<sup>38</sup> and were recorded as a function of wavelength, tunable between 7.4 and 15.0 eV in 100 meV steps. Absolute photon energy calibration and monochromator resolution (that resulted in VUV line width of 0.023 eV, full width at half-maximum (fwhm)) were determined using the atomic absorption line spectrum of an argon gas filter located between the light source and Beamline 9.0.2.3 end station and used to prevent higher harmonics of the desired photon energies to be transmitted to the end station. At each photon energy setting, 500 000 mass spectra were collected before moving the undulator and monochromator to the next photon energy setting. The ALS was maintained at a constant electron current of 500 mA using the top-off mode. The relative photon flux was monitored with a calibrated photodiode and is used to normalize the relative ion yields taken at different photon energies. Typical ion yields at  $\sim 9.3$  eV photon energies were on the order of hundreds up to a few thousands of ions/second, depending on the photon flux, whereas the typical background signal at mass peaks of interest was  $<1$  count/second.

**2.3. Aerosol Beam, Tunable VUV-PI-TOFMS.** The aerosol experimental apparatus at the Chemical Transformations Beamline 9.0.2.1 of the Advanced Light Source in Berkeley, CA, previously described in detail,<sup>7,30,34</sup> includes an aerosol particle generation system, a scanning-mobility particle

size (SMPS) analyzer, and an aerosol time-of-flight mass spectrometer (ATOFMS).

HEHN ionic liquid aerosols were generated by a constant output atomizer (TSI model 3076) from  $\sim 5$  g/L of HEHN in water solutions, and HEH aerosols were generated from  $\sim 8$  g/L in water solutions. The generated liquid droplets were then entrained in a nitrogen carrier gas at 10 psi and were dried by passing through a 1-m-long silica gel diffusion dryer tube. However, due to the increased vapor pressure of HEH, no HEH aerosols were detected using the drying tube approach, and so, for the case of generating HEH aerosols, the HEH aerosol flow was instead directly introduced into the aerosol mass spectrometer, and the presence of H<sub>2</sub>O in the HEH aerosols was determined to not affect the HEH thermal and catalytic decomposition chemistry. A portion of the aerosol flow was diverted to the SMPS. The aerosol particle size distribution and number density were measured using the SMPS consisting of a commercial differential mobility analyzer (DMA; TSI model 3081) coupled to a condensation particle counter (CPC; TSI model 3772). Aerosol particles of HEHN produced in our experiment had a median diameter of  $81 \pm 3$  nm and a total concentration of  $4.3 \times 10^6$  particles/cm<sup>3</sup>, while similarly produced aerosol particles of HEH had a median diameter of  $173 \pm 11$  nm and a total concentration of  $1.2 \times 10^7$  particles/cm<sup>3</sup>.

The chemical composition of the aerosols was measured using the ATOFMS, a custom-built, soft ionization vacuum ultraviolet aerosol mass spectrometer described by Gloaguen et al.<sup>35</sup> Briefly, a portion of the aerosol flow was sampled through a 500  $\mu$ m orifice coupled to an aerodynamic lens that focuses the particle beam and reduces the gas-phase molecular concentration by means of a pinhole plate system described by Liu et al.<sup>36</sup> Only particles with diameters  $>50$  nm were transmitted by the aerodynamic lens, and the particle flux entering the interaction region was estimated to be about  $3 \times 10^7$  particles/s.<sup>39</sup> Subsequently, inside the mass spectrometer, the particles were thermally or catalytically decomposed between 100 and 317 °C on a heated copper or iridium target in the ATOFMS ionization region, and products were vaporized and photoionized by tunable VUV radiation produced by the Chemical Transformations Beamline at the Advanced Light Source. The time-of-flight (TOF) mass spectra and ion yields of the aerosol decomposition products were measured with a pulsed TOF mass spectrometer and recorded as a function of the target temperature and the photon energy of the tunable VUV source. Mass spectra were taken as scans of the photon energy in the range from 7.4 to 15.0 eV, typically in 0.1 eV steps and averaged for 500 000 repeller pulses to improve the signal-to-noise ratio of the measured photoionization energy curves of the detected products.

In previous experimental work at the aerosol end station at the ALS Beamline 9.0.2.1, isolated ion pairs of aprotic ionic liquids were generated in the gas phase by thermal vaporization of IL aerosol particles on a heated copper target and were monitored using soft ionization detection with tunable vacuum ultraviolet (VUV) photoionization mass spectrometry.<sup>7,30</sup> However, in this case, HEHN is considered a protic ionic liquid, and thermal mass loss (vaporization) of this class of ionic liquids is generally assumed to occur via a proton transfer mechanism and vaporization of the resulting neutral species,<sup>2</sup> and this detail is discussed in the manuscript.

The ATOFMS was designed to promote flash vaporization, and, based on previously measured mass loss rates of ionic liquids and our measured aerosol mass flow rate into the ATOFMS, the residence and reaction time on the heated targets are estimated to be on the order of tens of microseconds before the volatile initial products are rapidly vaporized into the ionization region at  $\sim 10^{-6}$  Torr.<sup>6</sup> By integrating the photoion current over all photon energies and plotting the product photoion response as a function of target temperature, differences in the thermal decomposition (Cu target) versus catalytic decomposition chemistry (Ir target) can be evaluated.

#### 2.4. Nanotip Ambient Ionization Mass Spectrometry.

The nanotip ambient ionization mass spectrometer (NAIMS) setup has been described in detail previously.<sup>14</sup> Briefly, a HEHN/methanol solution (0.6% v/v) was deposited on an iridium surface on a hot plate (30–100 °C), and a plasma was generated by a DC bias between a tungsten nanotip (5.0  $\mu\text{m}$ ) and the metal surface. Mass spectra were obtained using an LTQ Orbitrap XL Hybrid Ion Trap-Orbitrap Mass Spectrometer from Thermo Fisher Scientific Inc. (resolution = 60 000 at  $m/z$  400 at a scan rate of 1 Hz). The nanotip–plate system was connected to the DC high-voltage supply; a 1 kV voltage was applied between the nanotip and the plate, and a 1 M $\Omega$  resistor was connected in the circuit for current limiting. The distance between the nanotip and the plate was adjusted to between 10 and 100  $\mu\text{m}$  to generate a continuous plasma. The ions produced by the plasma were collected in the mass spectrometer capillary probe that was biased at +50 V relative to the metal surface. The capillary tube provides the necessary pressure differential to sample at atmospheric pressure. The high resolution of the mass spectrometer allows for unambiguous determination of the atomic formulas of the product ions. Additionally, tandem mass spectrometry (MS-MS) was performed on product ions of interest to investigate the possible functional groups in the parent ions by analyzing their ion fragmentation patterns.

**2.5. Laser Desorption Ionization Droplet Delivery Mass Spectrometry.** An additional atmospheric pressure mass spectrometric technique, known as laser desorption/ionization droplet delivery mass spectrometry (LDIDD-MS), described elsewhere,<sup>15</sup> was also utilized to investigate HEHN on an iridium surface at room temperature and 150 °C. The LDIDD-MS system was built by combining a pulsed laser and an apparatus for generating droplets and coupled to the Orbitrap mass spectrometer described above. The cone and capillary voltages of the mass spectrometer inlet were set to 44 and 60 V, respectively. The capillary temperature was set to 275 °C. A voltage of 5 kV was applied to the metal tips of a syringe infused with solvent for droplet delivery. A DCR-11 pulsed Nd:YAG laser (Spectra Physics, CA) with a fundamental wavelength of 1064 nm was used to generate UV pulses. An HG-2 harmonic generator and PHS-1 harmonic separator were used to generate and separate the output of the UV laser at 266 nm. The UV laser beam was fired at 15 Hz and was aligned and focused using a 4-cm-focal-length lens on the sample surface. Dried N<sub>2</sub> gas was supplied at 80 psi to promote nebulization and generation of aerosol droplets, to propel the aerosols to the catalyst surface, and to deliver the analytes to the mass spectrometer inlet. A stream of liquid droplets generated by the nebulizing N<sub>2</sub> gas stream of the electrospray was tilted at 50–55° downward and directed onto the laser-irradiated region to capture desorbed molecules and molecular

ions from the substrate and deliver them to the inlet (using an extended capillary having a length of 9 cm) of the mass spectrometer. The electrospray source was placed at a distance of 3–5 mm from the focused laser spot. Either a 10% solution of HEHN in methanol was sprayed directly on the target surface or pure HEHN was placed on the target and a mixture of methanol and water (1:1, v/v) was used as a solvent for droplets. For the former case, solvent flow rate and pressure of N<sub>2</sub> gas supply were adjusted such that desorption solely by the liquid droplets was minimized. The optimal condition for LDIDD-MS was a flow rate of 0.5  $\mu\text{L}/\text{min}$  and a N<sub>2</sub> pressure of 80 psi. The diameter of the electrospray on the sample surface was around 200  $\mu\text{m}$ . The diameter of the focused laser beam at 266 nm was ideally 1.4  $\mu\text{m}$  and practically 2–3  $\mu\text{m}$ . The distance between the mass spectrometer inlet and the substrate was kept at 1 mm. The lateral distance between the mass spectrometer inlet and focused laser spot was adjusted to maximize the collected ion intensity ranging between 5 and 8 mm.

### 3. THEORY

Density functional theory (DFT) single-point energy calculations were performed at the M06/6-31+G(d,p)<sup>40</sup> level of theory (298 K, ZPVE-corrected) using the Gaussian 16 suite of programs.<sup>41</sup> Bond scans were performed, where the H atom was transferred from the original atom to the target atom in steps of 0.05 Å, while all other degrees of freedom were allowed to relax and the potential energy was minimized at each step. Relative enthalpies ( $\Delta H$ ) and free energies ( $\Delta G$ ) of stationary points, both local minima and transition states, have mean unsigned errors (MUEs) of typically less than 2.0 kcal/mol,<sup>40</sup> and the calculated ionization energies (IEs) and photoion appearance energies (AEs) are reported as  $\Delta G$  values with estimated errors of  $\pm 0.2$  eV. Born–Oppenheimer molecular dynamics (BOMD) simulations were performed at the PM6 level of theory, with the keywords `scf = qc`, `maxpoints = 400`, `step size = 10 000`, and `rtemp = 1500–6000 K`, and are described in more detail in the Supporting Information (SI), p S15–S25.

### 4. RESULTS/DISCUSSION

**4.1. Flash Pyrolysis VUV-PI-TOFMS.** The approach in the flash pyrolysis VUV-PI-TOFMS experiment presents several advantages: (1) a short reaction time to examine the initial steps of the thermal decomposition; (2) supersonic cooling to quench the reactions and minimize recombination of products and intermediates; and (3) minimal ion fragmentation by the use of the 10.45 eV “soft” photoionization source that imparts sufficient energy to ionize many closed-shell and free-radical species. The supersonic cooling further reduces photoionization fragmentation by minimizing the internal energy of the parent molecules and the pyrolysis products.

The literature regarding the thermal decomposition mechanism of HEH is sparse, and the only article that we could find indicated that HEH primarily decomposes at  $\sim 215$  °C to methylhydrazine and formaldehyde ( $\text{HOCH}_2\text{CH}_2\text{NHNH}_2 \rightarrow \text{H}_2\text{CO} + \text{H}_3\text{CNHNH}_2$ ), although traces of ethanolamine, ammonia, and hydrazine were also detected.<sup>42</sup> Ando et al. reported an exothermic decomposition of gaseous HEH by differential scanning calorimetry (DSC) at  $T_0 = 251.0$  °C and an associated heat of decomposition of  $Q = 240$  cal/g (76.3 kJ/mol), but no decomposition mechanism

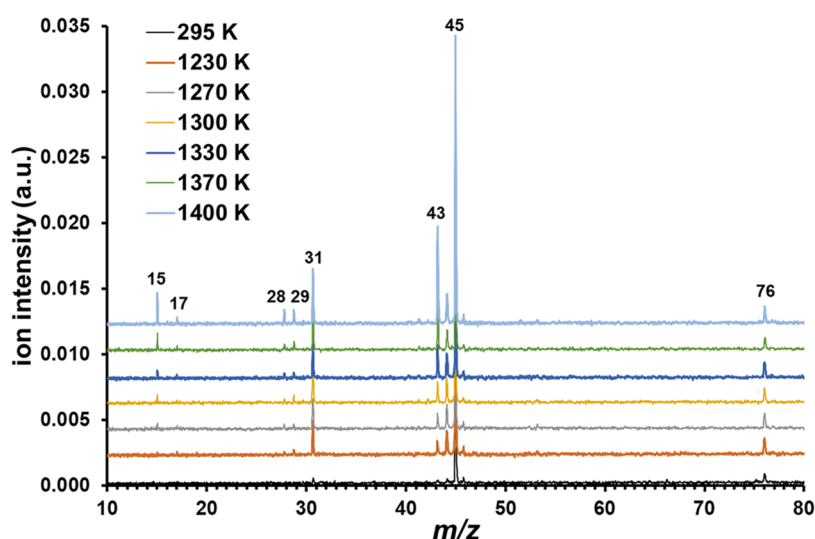


**Figure 1.** VUV-PI-TOFMS of HEH at 10.45 eV photon energy from 295 to 1400 K. The spectra have been offset for clarity.

was indicated.<sup>43</sup> A related article using high-resolution mass spectrometry indicated that the C–C bond dissociation (BD) of the related cationic  $\text{HEH}^+$  to form  $\text{HOCH}_2$  and  $\text{CH}_2\text{NHNH}_2^+$  is possible, with an appearance energy of 9.1 eV for  $\text{CH}_2\text{NHNH}_2^+$ , and that  $\text{CH}_2\text{NHNH}_2^+$  is unstable when neutralized.<sup>44</sup> The literature mass spectrum (electron-impact ionization) of HEH indicates mass fragment peaks at  $m/z$  45 (100%) and 31 (10%) and smaller peaks at  $m/z$  15, 17–19, 26–32, 39–46, and 55–59.<sup>45</sup>

The thermal decomposition of HEH by flash pyrolysis between 295 and 1400 K can be seen in Figure 1. At 295 K, masses at  $m/z$  76 and 45 correspond to the parent HEH and the dissociative photoionization product  $\text{CH}_2\text{NHNH}_2^+$ ,<sup>44</sup> respectively, and a very small peak at  $m/z$  31 is observed. At 1230 K, significant peaks appear at  $m/z$  44, 43, and 31 and smaller peaks at  $m/z$  28 and 29. Above 1300 K, there are additional peaks at  $m/z$  15 and 17. To explain the peaks observed in Figure 1, a systematic series of DFT calculations of the enthalpies ( $\Delta H_{298}$ ) and free energies of reaction ( $\Delta G_{298}$ ), ionization energies (IEs), and dissociative photoionization appearance energies (AEs) are compiled in Table 1, and these calculations are discussed in detail below.

First, let us look at the unimolecular thermal decomposition of the simpler methylhydrazine system that has been studied both experimentally<sup>46</sup> and theoretically<sup>47</sup> and has been shown to produce a combination of free radicals and molecular species with activation barriers of around 63.1–69.5 kcal/mol (264.0–290.8 kJ/mol). If the primary unimolecular thermal decomposition of HEH produced methylhydrazine ( $m/z$  46, IE = 7.7 eV) and  $\text{H}_2\text{CO}$  ( $m/z$  30, IE = 10.9 eV; not ionized at 10.45 eV), as suggested in ref 42, intact methylhydrazine would exhibit significant peaks in the mass spectrum at  $m/z$  45 and 46 and a smaller  $m/z$  31 peak (Figure 1, top in ref 48). If the methylhydrazine is produced with enough internal energy to further decompose, there would be a series of peaks at  $m/z$  15, 17, 28, 29, 30, and 31 (Figure 1, bottom in ref 48). However, since there are no significant  $m/z$  46 or 30 peaks apparent in Figure 1, the formation of methylhydrazine is negligible (<1%) under our experimental conditions. Perhaps, the pronounced formation of methylhydrazine in ref 42 was a result of surface reactions with the sample container walls.

In assessing the unimolecular thermal decomposition of HEH using density functional theory (at the M06/6-31+G-(d,p) level), a systematic approach to identify the lowest activation barrier pathways was utilized that included all possible elementary reactions, and the results are reported in Table 1 (reactions 1–32) in order of increasing activation barrier—either as transition state enthalpy,  $\Delta H_{298}^\ddagger$ , or the bond dissociation enthalpy (BDE). In Table 1, the reaction types are identified as simple bond dissociations (BDs), hydrogen transfer (e.g., OH to C1) reactions, and  $\text{H}_2$  eliminations ( $\text{H}_2$  elim.). Possible secondary reactions (2°, reactions 34–43) and photoionization processes (reactions 44–70) are also included in Table 1. It is noted here that the simple bond dissociations and any  $\text{H}_2$  elimination pathways identified all have activation barriers that are too high to proceed ( $\geq \sim 275$  kJ/mol) and are not believed to be accessible in this experimental setup. The systematic DFT approach and results are described in detail below.

First, the structures of the lowest-energy isomers were determined. In contrast to methylhydrazine, HEH has more isomers possible due to rotations around the bonded heteroatoms, and the lowest-energy isomer is identified as a five-membered cyclic structure with the OH group hydrogen, hydrogen-bonded to N1 (HEH0; Figure 2). A slightly higher-energy structure was located that has a six-membered cyclic structure with the NH of the terminal nitrogen (N2) hydrogen-bonded to the oxygen (HEH1; Figure 2). While there are multiple low-energy HEH structures that can lead directly to bond fission processes, the structure HEH1 has the lowest direct barriers to decomposition products and all energies in Figure 2 are calculated relative to HEH1.

Second, the simple bond dissociation energies (BDEs) were assessed (Figure 2 and reactions 6, 8, 17, 19, 21, 26, and 28–30, Table 1). It can be seen that the enthalpies ( $\Delta H_{298}$ ) of bond dissociation of the N–N and C–N bonds, yielding products with masses of 16 and 60 amu (reaction 6) and 31 and 45 amu (reaction 8) in HEH, are very similar: 268.2 and 274.3 kJ/mol, while for C–C (product masses 31 and 45 amu, reaction 19) and C–O (product masses 17 and 59, reaction 28) bond cleavages, they are higher in energy at 335.9 and 393.0 kJ/mol, respectively. In the mass spectra in Figure 1, there is no indication of the formation of  $m/z$  60 or 59 peaks

**Table 1.** Elementary Reactions of HEH Unimolecular Thermal Decomposition Performed at the M06/6-31+G(d,p) Level of Theory<sup>f</sup>

reaction class	reaction	$E_a$ (kJ/mol)	$\Delta H_{298}$ (kJ/mol)	$\Delta G_{298}$ (kJ/mol)	$\Delta H_{298}^\ddagger$ (kJ/mol)	$\Delta G_{298}^\ddagger$ (kJ/mol)	product <i>m/z</i>
OH <sup>a</sup> to N1	HEH + $\Delta$ → HOCH <sub>2</sub> CH <sub>2</sub> N <sup>+</sup> H <sub>2</sub> N <sup>-</sup> H (OH to N1, then N2H to O) (1)	173.4	152.5	154.7	173.4	178.0	76
OH to N2	HEH + $\Delta$ → H <sub>2</sub> CO + H <sub>2</sub> C=NH + NH <sub>3</sub> (2)	236.0	4.8	-24.2	236.0	235.7	30, 29, 17
N1H to N2	HEH + $\Delta$ → HOCH <sub>2</sub> CH <sub>2</sub> N <sup>-</sup> N <sup>+</sup> H <sub>3</sub> (3)	249.0	163.5	163.8	249.0	248.2	76
N2H to N1	HEH + $\Delta$ → HOCH <sub>2</sub> CH <sub>2</sub> N <sup>+</sup> H <sub>2</sub> N <sup>-</sup> H (4)	254.1	153.6	155.9	254.1	255.6	76
N1H to C1	HEH + $\Delta$ → HOCH <sub>2</sub> CH <sub>3</sub> + H <sub>2</sub> N=N (5)	255.3	120.8	109.7	255.3	254.2	46, 30
BD <sup>b</sup> NN	HEH + $\Delta$ → HOCH <sub>2</sub> CH <sub>2</sub> ÑH + •NH <sub>2</sub> (6)	268.2	268.2	214.3			60, 16
C1H to N2	HEH + $\Delta$ → HOCH <sub>2</sub> CH=NH + NH <sub>3</sub> (7)	270.2	-79.9	-92.6	270.2	271.4	59, 17
BD CN	HEH + $\Delta$ → HOCH <sub>2</sub> ĊH <sub>2</sub> + HÑNH <sub>2</sub> (8)	274.3	274.3	216.1			45, 31
C2H to N2	HEH + $\Delta$ → HOCH=CH <sub>2</sub> + H <sub>3</sub> N <sup>+</sup> N <sup>-</sup> H (9)	275.0	265.8	213.7	275.0	272.4	44, 32
C2H to N1	HEH + $\Delta$ → HOCH=CH <sub>2</sub> + H <sub>2</sub> N=NH <sub>2</sub> (10)	282.4	57.7	41.2	282.4	284.4	44, 32
C1H to O	HEH + $\Delta$ → H <sub>2</sub> O + H <sub>2</sub> C=CHNHNH <sub>2</sub> (11)	290.5	32.6	16.4	290.5	288.1	18, 58
N2 H2 elim	HEH + $\Delta$ → H <sub>2</sub> + HOCH <sub>2</sub> CH <sub>2</sub> NHN (12)	295.2	176.7	141.5	295.2	296.3	2, 74
N2H to C2	HEH + $\Delta$ → HOCH <sub>3</sub> + H <sub>2</sub> ĊNHÑH (13)	297.8	136.0	118.2	297.8	297.0	32, 44
N1H to O	HEH + $\Delta$ → H <sub>2</sub> O + H <sub>2</sub> ĊH <sub>2</sub> ÑNH <sub>2</sub> (14)	301.9	53.8	42.6	301.9	301.0	18, 58
C1H to N1	HEH + $\Delta$ → HOCH <sub>2</sub> C <sup>-</sup> HN <sup>+</sup> H <sub>2</sub> NH <sub>2</sub> (15)	310.8	222.0	219.2	310.8	309.7	76
C1 H2 elim	HEH + $\Delta$ → H <sub>2</sub> + HOCH <sub>2</sub> ĊNHNH <sub>2</sub> (16)	321.4	229.7	189.2	321.4	320.4	2, 74
BD N1H	HEH + $\Delta$ → HOCH <sub>2</sub> CH <sub>2</sub> ÑNH <sub>2</sub> + H• (17)	325.7	325.7	287.9			75, 1
C2H to O	HEH + $\Delta$ → H <sub>2</sub> OCHCH <sub>2</sub> NHNH <sub>2</sub> (18)	330.9	317.8	315.9	330.9	315.9	76
BD CC	HEH + $\Delta$ → HOĊH <sub>2</sub> + H <sub>2</sub> ĊNHNH <sub>2</sub> (19)	335.9	335.9	278.5			31, 45
C2H to C1	HEH + $\Delta$ → HOĊH + H <sub>3</sub> CNHNH <sub>2</sub> (20)	341.1	240.6	231.2	341.1	335.0	30, 46
BD N2H	HEH + $\Delta$ → HOCH <sub>2</sub> CH <sub>2</sub> NHNÑH + H• (21)	341.6	341.6	301.7			75, 1
C2 H2 elim	HEH + $\Delta$ → H <sub>2</sub> + HOĊCH <sub>2</sub> NHNH <sub>2</sub> (22)	351.6	280.1	243.7	351.6	352.3	2, 74
N1H to C2	HEH + $\Delta$ → HOCH <sub>3</sub> + H <sub>2</sub> C=NNH <sub>2</sub> (23)	354.6	62.6	37.0	354.6	350.8	32, 44
OH to C2	HEH + $\Delta$ → O=CHCH <sub>2</sub> NHNH <sub>2</sub> + H <sub>2</sub> (24)	357.4	83.5	68.4	357.4	356.8	74, 2
N2H to O	HEH + $\Delta$ → H <sub>2</sub> O + H <sub>2</sub> CCH <sub>2</sub> + HNNH (25)	368.8	107.0	76.8	368.8	368.9	18, 28, 30
BD C1H	HEH + $\Delta$ → HOCH <sub>2</sub> ĊHNHNH <sub>2</sub> + H• (26)	378.0	378.0	338.8			75, 1
OH to C1	HEH + $\Delta$ → H <sub>2</sub> CO + H <sub>2</sub> + HĊNHNH <sub>2</sub> (27)	379.7	68.0	51.1	379.7	364.6	32, 2, 42
BD CO	HEH + $\Delta$ → HO• + H <sub>2</sub> ĊCH <sub>2</sub> NHNH <sub>2</sub> (28)	393.0	393.0	344.1			17, 59
BD C2H	HEH + $\Delta$ → HOĊHCH <sub>2</sub> NHNH <sub>2</sub> + H• (29)	393.2	393.2	355.1			75, 1
BD OH	HEH + $\Delta$ → •OCH <sub>2</sub> CH <sub>2</sub> NHNH <sub>2</sub> + H• (30)	404.5	404.5	370.8			75, 1
C1H to C2	HEH + $\Delta$ → HOCH=CHNHNH <sub>2</sub> + H <sub>2</sub> (31)	438.8	120.6	106.7	438.8	437.4	74, 2
N2H to C1	HEH + $\Delta$ → H <sub>2</sub> + HOCH <sub>2</sub> ĊNHNÑH (32)	440.4	176.9	159.1	440.4	438.1	2, 74
N1 N2 H2 elim	HEH + $\Delta$ → H <sub>2</sub> + HOCH <sub>2</sub> CH <sub>2</sub> N=NH (33)	449.1	122.4	102.5	449.1	448.0	
2° <sup>c</sup>	HOCH <sub>2</sub> CH <sub>2</sub> N <sup>+</sup> H <sub>2</sub> N <sup>-</sup> H + $\Delta$ → HOCH <sub>2</sub> CH <sub>3</sub> + HNNH (34)	192.3	-80.7	-133.4	192.3	182.1	46, 30
2°	HOCH <sub>2</sub> CH <sub>3</sub> + $\Delta$ → H <sub>3</sub> CĊH + H <sub>2</sub> O (35)	327.0	352.4	307.9	327.0	323.8	28, 18
2°	HOCH <sub>2</sub> CH <sub>3</sub> + $\Delta$ → •CH <sub>3</sub> + H <sub>2</sub> ĊOH (36)	362.2	362.2	312.4			15, 31
2°	HOCH <sub>2</sub> CH <sub>3</sub> + $\Delta$ → •C <sub>2</sub> H <sub>5</sub> + •OH (37)	389.7	389.7	340.0			29, 17
2°	HOCH <sub>2</sub> CH <sub>3</sub> + $\Delta$ → O=CHCH <sub>3</sub> + H <sub>2</sub> (38)	345.8	68.7	31.7	345.8	347.1	44, 2
2°	H <sub>2</sub> N=N: + $\Delta$ → N <sub>2</sub> + H <sub>2</sub> (39)	240.9	-244.9	-274.1	240.9	239.9	28, 2
2°	H <sub>2</sub> N=N: + $\Delta$ → HNNH (40)	202.1	-81.6	-79.9	202.1	201.1	30
2°	HNNH + $\Delta$ → HNN• + H• (41)	270.0	270.0	234.0			29, 1
2°	H <sub>3</sub> CCH + $\Delta$ → H <sub>2</sub> CCH <sub>2</sub> (42)	7.6	-287.9	-288.2	7.6	7.5	28
2°	HNNH + $\Delta$ → N <sub>2</sub> + H <sub>2</sub> (43)						28, 2

Table 1. continued

reaction class	reaction	product <i>m/z</i>	IE/AE (eV)
PI <sup>d</sup>	HEH + <i>hν</i> → HEH <sup>+</sup> + e <sup>-</sup> (44)	76	7.5
dissoc PI <sup>e</sup>	HEH + <i>hν</i> → H <sub>2</sub> CNHNH <sub>2</sub> <sup>+</sup> + HOCH <sub>2</sub> + e <sup>-</sup> (45)	45	8.8
dissoc PI	HEH + <i>hν</i> → H <sub>2</sub> CNHNH <sub>2</sub> + HOCH <sub>2</sub> <sup>+</sup> + e <sup>-</sup> (46)	31	10.4
dissoc PI	HEH + <i>hν</i> → HOCH <sub>2</sub> CH <sub>2</sub> <sup>+</sup> + N <sub>2</sub> H <sub>3</sub> + e <sup>-</sup> (47)	45	8.6
dissoc PI	HEH + <i>hν</i> → HOCH <sub>2</sub> CH <sub>2</sub> + N <sub>2</sub> H <sub>3</sub> <sup>+</sup> + e <sup>-</sup> (48)	31	10.0
dissoc PI	HEH + <i>hν</i> → OCH <sub>2</sub> CH <sub>2</sub> <sup>+</sup> + N <sub>2</sub> H <sub>4</sub> + e <sup>-</sup> (49)	44, 32	9.8
dissoc PI	HEH + <i>hν</i> → HOCHCH <sub>2</sub> <sup>+</sup> + N <sub>2</sub> H <sub>4</sub> + e <sup>-</sup> (50)	44, 32	9.2
dissoc PI	HEH + <i>hν</i> → HOCH <sub>2</sub> CH <sup>+</sup> + N <sub>2</sub> H <sub>4</sub> + e <sup>-</sup> (51)	44, 32	11.3
dissoc PI	HEH + <i>hν</i> → OCH <sub>2</sub> CH <sub>2</sub> <sup>+</sup> + H + N <sub>2</sub> H <sub>3</sub> + e <sup>-</sup> (52)	44, 31, 1	12.9
dissoc PI	HEH + <i>hν</i> → HOCHCH <sub>2</sub> <sup>+</sup> + H + N <sub>2</sub> H <sub>3</sub> + e <sup>-</sup> (53)	44, 31, 1	12.4
dissoc PI	HEH + <i>hν</i> → HOCH <sub>2</sub> CH <sup>+</sup> + H + N <sub>2</sub> H <sub>3</sub> + e <sup>-</sup> (54)	44, 31, 1	14.5
PI	CH <sub>3</sub> + <i>hν</i> → CH <sub>3</sub> <sup>+</sup> + e <sup>-</sup> (55)	15	
PI	NH <sub>2</sub> + <i>hν</i> → NH <sub>2</sub> <sup>+</sup> + e <sup>-</sup> (56)	16	12.5
PI	OH + <i>hν</i> → OH <sup>+</sup> + e <sup>-</sup> (57)	17	16.1
PI	NH <sub>3</sub> + <i>hν</i> → NH <sub>3</sub> <sup>+</sup> + e <sup>-</sup> (58)	17	10.1
PI	H <sub>2</sub> O + <i>hν</i> → H <sub>2</sub> O <sup>+</sup> + e <sup>-</sup> (59)	18	12.6
PI	HCNH + <i>hν</i> → HCNH <sup>+</sup> + e <sup>-</sup> (60)	28	7.3
PI	H <sub>2</sub> CN + <i>hν</i> → H <sub>2</sub> CN <sup>+</sup> + e <sup>-</sup> (61)	28	10.5 (vt)
PI	C <sub>2</sub> H <sub>4</sub> + <i>hν</i> → C <sub>2</sub> H <sub>4</sub> <sup>+</sup> + e <sup>-</sup> (62)	28	10.5
PI	H <sub>2</sub> CNH + <i>hν</i> → H <sub>2</sub> CNH <sup>+</sup> + e <sup>-</sup> (63)	29	9.8
PI	NO + <i>hν</i> → NO <sup>+</sup> + e <sup>-</sup> (64)	30	9.3
PI	N <sub>2</sub> H <sub>3</sub> + <i>hν</i> → N <sub>2</sub> H <sub>3</sub> <sup>+</sup> + e <sup>-</sup> (65)	31	7.8
PI	N <sub>2</sub> H <sub>4</sub> + <i>hν</i> → N <sub>2</sub> H <sub>4</sub> <sup>+</sup> + e <sup>-</sup> (66)	32	7.9
PI	H <sub>2</sub> CO + <i>hν</i> → H <sub>2</sub> CO <sup>+</sup> + e <sup>-</sup> (67)	32	10.9
PI	H <sub>3</sub> CNHNH <sub>2</sub> + <i>hν</i> → H <sub>3</sub> CNHNH <sub>2</sub> <sup>+</sup> + e <sup>-</sup> (68)	46	7.7
PI	CH <sub>2</sub> CH <sub>2</sub> HNNH <sub>2</sub> + <i>hν</i> → CH <sub>2</sub> CH <sub>2</sub> HNNH <sub>2</sub> <sup>+</sup> + e <sup>-</sup> (69)	59	9.6
PI	HOCH <sub>2</sub> CH <sub>2</sub> HN + <i>hν</i> → HOCH <sub>2</sub> CH <sub>2</sub> HN <sup>+</sup> + e <sup>-</sup> (70)	60	10.1 (vt)

<sup>a</sup>OH to N1 refers to OH hydrogen transfer to nitrogen 1, etc. <sup>b</sup>BD NN refers to dissociation of the N–N bond, etc. <sup>c</sup>Refers to reactions of products. <sup>d</sup>Refers to photoionization. <sup>e</sup>Refers to dissociative photoionization. <sup>f</sup>Mean unsigned errors are <±2.0 kcal/mol (<±8.4 kJ/mol).

corresponding to the larger fragments in the N–N (reaction 6) and C–O (reaction 28) bond cleavages that would be expected to be ionized at 10.45 eV (IE(HOCH<sub>2</sub>CH<sub>2</sub>NH, *m/z* 60) = 10.1 eV (vertical IE, M06); IE(CH<sub>2</sub>CH<sub>2</sub>NHNH<sub>2</sub>, *m/z* 59) = 9.6 eV). While the enthalpy of the C–O bond cleavage is prohibitively high (393.0 kJ/mol, reaction 28), it is noted that no *m/z* 60 product stemming from the N–N bond cleavage (HOCH<sub>2</sub>CH<sub>2</sub>NH, reaction 6) is detected even though the enthalpy barrier is similar to the C–N cleavage channel (reaction 8). Therefore, it is unlikely that the thermally activated bond dissociation between the heteroatoms is occurring under these experimental conditions. The lack of *m/z* 75 in Figure 1 also indicates that H-fission processes (reactions 17, 21, 26, 29, and 30) are not occurring.

Third, the energetics of possible hydrogen transfer reactions were investigated by running bond scans between each hydrogen and the target heteroatom (O, C1, etc.). Remember that HEH1 is a six-membered ring with the terminal NH hydrogen-bonded to the oxygen. By far, the lowest-energy barrier pathway ( $\Delta H^\ddagger = 173.4$  kJ/mol, reaction 1) involves a hydrogen transfer from O to N1, followed by a spontaneous

second hydrogen transfer from N2 to O, leading to the formation of HOCH<sub>2</sub>CH<sub>2</sub>N<sup>+</sup>H<sub>2</sub>N<sup>-</sup>H (Figure 1a). This product remains as *m/z* 76 and therefore is not discernible from the HEH (reactant) by this experimental method. Nevertheless, possible reactivity of this isomer will be discussed below. The next highest activation barrier pathway involves a transition state (TS3; Figure 2) having a single imaginary frequency where the OH hydrogen transfers to the terminal nitrogen (N2) leading to NH<sub>3</sub> elimination (reaction 2). The calculated internal reaction coordinate for this transition state leads to not only NH<sub>3</sub> production but also the spontaneous dissociation of the OCH<sub>2</sub>–CH<sub>2</sub>NH cofragment to form the stable, closed-shell species H<sub>2</sub>CO and H<sub>2</sub>C=NH (IE = 9.88 ± 0.07<sup>49</sup>). The enthalpy for this transition state is  $\Delta H^\ddagger = 236.0$  kJ/mol, significantly lower than for any of the bond fission processes mentioned above and for any of the thermal decomposition processes of methylhydrazine mentioned above.<sup>42</sup> On the other hand, OH hydrogen to N1 followed by dissociation could lead to H<sub>2</sub>COCH<sub>2</sub> (ethylene oxide, IE = 10.56 ± 0.01 eV<sup>45</sup>) and N<sub>2</sub>H<sub>4</sub> (IE = 8.1 ± 0.15 eV<sup>45</sup>), the latter of which would be easily detectable in our setup at *m/z*

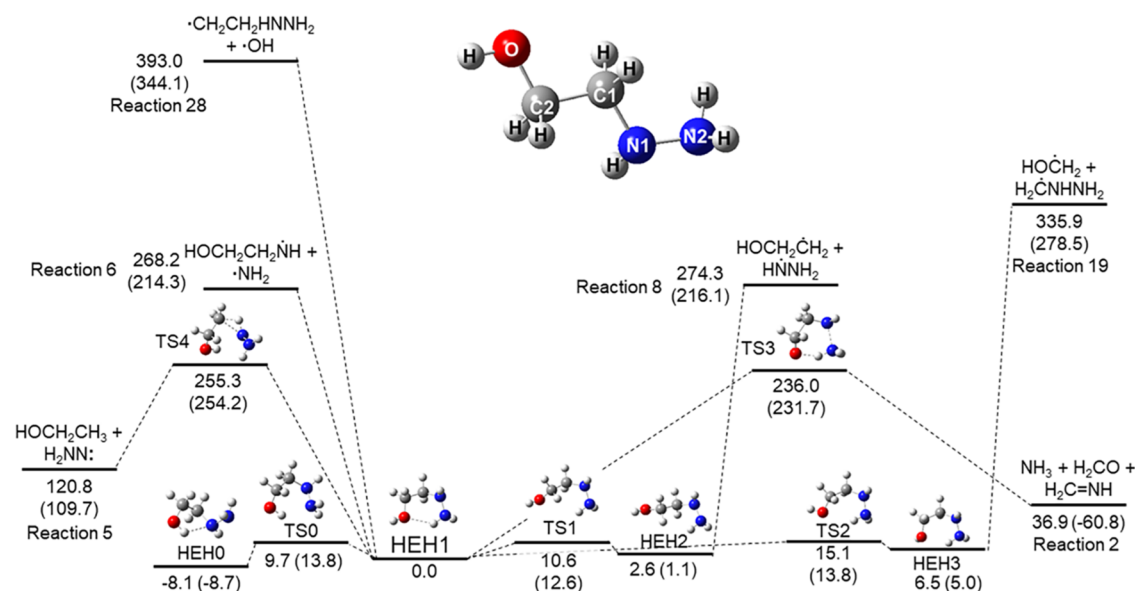


**Figure 2.** Atomic numbering and HEH thermal decomposition reaction profile.  $\Delta H_{298}^{\ddagger}$  ( $\Delta G_{298}^{\ddagger}$ ) values calculated in kJ/mol at the M06/6-31+G(d,p) level of theory are relative to HEH1. Reaction numbers are from Table 1.

32. Figure 1 shows a complete lack of the signal at  $m/z$  32 ( $S/N < 2$ ); hence, this pathway may be ruled out.

The OH hydrogen to N2 pathway of reaction 2 leading to  $\text{NH}_3$ ,  $\text{H}_2\text{CNH}$ , and  $\text{H}_2\text{CO}$  could account for the detection of  $m/z$  17 and 29 above  $T = 1230$  K, although the  $\text{H}_2\text{CO}$  product is not detected due to its higher photoionization threshold. Other low-barrier hydrogen transfer processes leading to stable stationary state HEH isomers include H transfer between C1, N1, and N2 (reactions 3, 4, and 7). Reaction 5 involves H transfer from N1 to C1 and leads to the formation of  $\text{HOCH}_2\text{CH}_3 + \text{H}_2\text{N}=\text{N}$ , and this pathway will be discussed in more detail below.

In the bond scans that were performed in the search for transition states for H transfer reactions, several transition states were instead located for  $\text{H}_2$  elimination processes. These resulted in  $\text{H}_2$  elimination reactions from O–C1, O–C2, C1–C2, or N2–C1, respectively (reactions 27, 24, 31, and 32), having substantial enthalpy barriers ( $\Delta H^{\ddagger} > 350$  kJ/mol) similar to hydrogen BDEs (reactions 17, 21, 26, 29, and 30), and this explains the lack of a peak at  $m/z$  74. No direct transition state was located in the bond scan between the OH hydrogen and C1 to produce  $\text{H}_2\text{CO}$  and  $\text{H}_3\text{CNHNH}_2$  but instead yielded a transition state for  $\text{H}_2$  elimination, with one H from O and one H from C1, resulting in  $\text{H}_2\text{CO} + \text{H}_2 + \text{HCNHNH}_2$ ,  $\Delta H^{\ddagger} = 379.7$  kJ/mol (reaction 27), and this route is not accessible in this experiment. Attempts to locate a direct transition state between HEH and  $\text{H}_2\text{CO} + \text{H}_3\text{CNHNH}_2$  by investigating the reverse reaction:  $\text{H}_2\text{CO} + \text{H}_3\text{CNHNH}_2 \rightarrow \text{HOCH}_2\text{CH}_2\text{NHNH}_2$  always converged to the same  $\text{H}_2$  elimination saddle point as reaction 27, with  $\Delta H^{\ddagger} = 379.7$  kJ/mol. A possible HEH unimolecular decomposition pathway to produce  $\text{H}_3\text{CNHNH}_2 + \text{HOCH}$  (reaction 20,  $\Delta H^{\ddagger} = 341.1$  kJ/mol) was identified, but the high barrier also precludes this route. Since, at this level of theory, no direct H-migration transition state was located for the elementary unimolecular decomposition of HEH to form  $\text{H}_2\text{CO}$  and  $\text{H}_3\text{CNHNH}_2$  (OH hydrogen to C1), this could suggest that the  $\text{H}_2\text{CO}$  and  $\text{HOCH}_2\text{CH}_2\text{NH}_2$  products observed in ref 42 were formed through a heterogeneous pathway, although higher-level

quantum calculations may be able to locate this possible transition state. It should be noted that, in the BOMD simulations, multiple trajectories resulted in  $\text{H}_3\text{CNHNH}_2$  formation plus  $\text{HCOH}$ , but when these trajectories were analyzed in detail, they appeared to first proceed through a C1–C2 bond cleavage with subsequent H-abstraction from OH by carbon in the leaving  $\text{H}_2\text{CNHNH}_2$  radical to give  $\text{H}_3\text{CNHNH}_2$ . This reaction has a barrier that is likely similar or higher in energy than the C1–C2 bond cleavage energy ( $\Delta H = 335.9$  kJ/mol, reaction 19).

In Table 1, when comparing elementary reactions with the lowest enthalpy barriers  $\Delta H^{\ddagger}$  or  $\Delta H$  for the bond dissociation (BD), the next highest enthalpy barriers above that for O hydrogen transfer to N2 (reaction 2) mentioned earlier are for the hydrogen migrations between the nitrogens: N2 hydrogen  $\rightarrow$  N1,  $\Delta H^{\ddagger} = 254.1$  kJ/mol (reaction 4) and N1 hydrogen  $\rightarrow$  N2,  $\Delta H^{\ddagger} = 249.0$  kJ/mol (reaction 3), resulting in stationary points that are high-energy structural isomers of HEH that cannot be experimentally differentiated from HEH at  $m/z$  76. Next, the N1H to C1 hydrogen transfer resulting in  $\text{HOCH}_2\text{CH}_3 + \text{H}_2\text{N}=\text{N}$ : has a similar barrier of  $\Delta H^{\ddagger} = 255.3$  kJ/mol (reaction 5; Figure 2), and this channel will be discussed in detail below. Formation of  $\text{HOCH}_2\text{CH}_3 + \text{HNNH}$  is also possible via N1H to C1 (reaction 34) in the structural isomer  $\text{HOCH}_2\text{CH}_2\text{N}^+\text{H}_2\text{N}^-\text{H}$  formed in reactions 1 and 4 but with a higher enthalpy barrier of  $\Delta H^{\ddagger} = 344.8$  kJ/mol (Figure S1a).

Above the  $\text{HEH1} \rightarrow \text{HOCH}_2\text{CH}_3 + \text{H}_2\text{N}=\text{N}$ : reaction channel (reaction 5,  $\Delta H^{\ddagger} = 255.3$  kJ/mol), the next highest enthalpy barrier pathways are the N–N and C–N bond cleavages,  $\Delta H^{\ddagger} = 268.2$  (reaction 6) and  $\Delta H^{\ddagger} = 274.3$  kJ/mol (reaction 8), respectively, and since no photoions were detected ( $S/N < 2$ ) that correspond to the  $m/z$  60 species produced through the N–N cleavage, it is likely that these pathways are not accessed under these experimental conditions. Similarly, all of the other H-migration,  $\text{H}_2$  elimination, and BD pathways identified in Table 1 have higher barriers and are not likely activated under these experimental conditions.

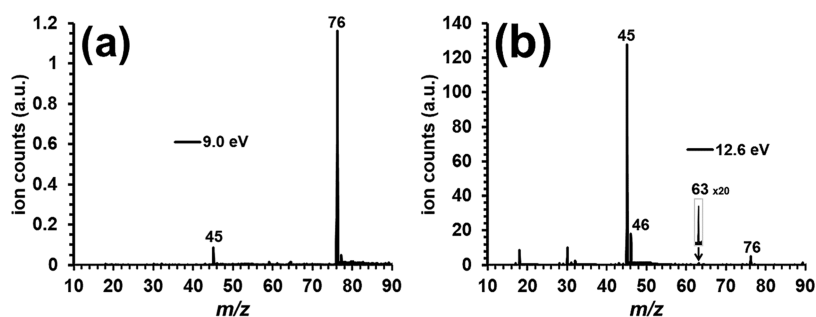


**Figure 3.** VUV-PI mass spectra of HEHN from the VUV-PI-TOFMS effusive source at 200 °C and at (a) 9.0 eV and (b) 12.6 eV photoionization energies, indicating the formation of HEH ( $m/z$  76) and  $\text{HNO}_3$  ( $m/z$  63). Also see Figure S5.

To explore the possibility of  $\text{HOCH}_2\text{CH}_3$  formation, flash pyrolysis of  $\text{HOCH}_2\text{CH}_3$  was performed at up to  $T = 1270$  K, and the results are shown in Figure S2. Although the literature IE values for  $\text{HOCH}_2\text{CH}_3$  range from 10.4 to 10.7 eV,<sup>50</sup> at 295 K, the parent peak at  $m/z$  46 is seen, indicating that  $\text{HOCH}_2\text{CH}_3$  can be photoionized using this technique. At  $T = 720$  K, a small peak is observed at  $m/z$  44, indicating  $\text{H}_2$  loss. At 1090 K,  $m/z$  15 appears, indicating the formation of the  $\cdot\text{CH}_3$  radical. At the highest temperature, 1270 K, the appearance of a small peak at  $m/z$  28 is observed, perhaps indicating the formation of  $\text{H}_2\text{CCH}_2$  or  $\text{H}_3\text{C}\dot{\text{C}}\text{H}$ .

The pyrolysis of  $\text{HOCH}_2\text{CH}_3$  (ethanol) has been studied extensively<sup>51–53</sup> and has a high-pressure thermal decomposition onset temperature of  $\sim 700$  K. The accepted mechanism proceeds primarily through three channels, reactions 35–37 (see Table 1):<sup>53</sup>



A fourth channel— $\text{HOCH}_2\text{CH}_3 \rightarrow \text{O}=\text{CHCH}_3 + \text{H}_2$  (reaction 38)—with a similar activation barrier to the  $\text{CH}_3 + \text{H}_2\text{COH}$  channel is also possible.<sup>53,54</sup> The 10.45 eV ionizing photons in our experiment should photoionize the products  $\text{H}_3\text{CCH}$  ( $m/z$  28, IE = 8.3 eV, M06),  $\text{CH}_3$  ( $m/z$  15, IE = 9.84 eV<sup>50</sup>),  $\text{C}_2\text{H}_5$  ( $m/z$  29, IE = 8.1 eV<sup>43</sup>),  $\text{H}_2\text{COH}$  ( $m/z$  31, IE = 7.56 eV,<sup>55</sup> with AE = 8.61 for  $m/z$  29,  $\text{CHO}^+$ <sup>55</sup>), and  $\text{O}=\text{CHCH}_3$  ( $m/z$  44 IE = 10.23 eV<sup>50</sup>) and possibly any hot  $\text{H}_2\text{CCH}_2$  ( $m/z$  28 IE = 10.51 eV<sup>50</sup>) as well as the parent product  $\text{HOCH}_2\text{CH}_3$  ( $m/z$  46, IE = 10.4–10.7 eV<sup>50</sup>), whereas the  $\text{H}_2\text{O}$ ,  $\text{OH}$ , and  $\text{H}_2$  all have IEs that are too high for photoionization at 10.45 eV. It is reported in the literature that  $\text{O}=\text{CHCH}_3$  can fragment to  $\text{C}_2\text{H}_3\text{O}^+ + \text{H}$  at an appearance energy of as low as  $10.50 \pm 0.05$  eV,<sup>56</sup> and this could account for the detection of  $m/z$  43 in Figure 1. Additionally, in the BOMD molecular dynamics simulations of HEH1 ( $T = 3000$ – $5500$  K, PM6, described in detail in the SI), 0.67% of the reactive pathways lead to  $\text{HOCH}_2\text{CH}_3 + \text{H}_2\text{N}=\text{N}:\text{HNNH}$  products, and starting from the  $\text{HOCH}_2\text{CH}_2\text{N}^+\text{H}_2\text{N}^-\text{H}$  intermediate (formed via reactions 1 and 4), 12.0% of the reactions lead to  $\text{HOCH}_2\text{CH}_3 + \text{HNNH}$ .

Additional discussions on  $\text{N}_2\text{H}_2$  isomerization, the analysis of relative peak intensities and possible contributions to the thermal decomposition of  $\text{HOCH}_2\text{CH}_3$ , literature rate constant analysis on the thermal decomposition of  $\text{HOCH}_2\text{CH}_3$ ,  $\text{H}_3\text{CCH}$  to  $\text{H}_2\text{CCH}_2$  isomerization, and thermal

contributions to the ionization energies of the possible products are included in the SI, p S3–S5.

In summary, we propose that the flash pyrolysis of HEH results can be explained by two main pathways: (1) OH hydrogen to  $\text{N}_2$  migration yielding  $\text{NH}_3$  ( $m/z$  17),  $\text{H}_2\text{CO}$  (not detected), and  $\text{H}_2\text{C}=\text{NH}$  ( $m/z$  29) and (2)  $\text{N1H}$  hydrogen to  $\text{C1}$  migration from HEH1 (or  $\text{HOCH}_2\text{CH}_2\text{N}^+\text{H}_2\text{N}^-\text{H}$ ) to form  $\text{HOCH}_2\text{CH}_3$  that further decomposes to  $\text{CH}_3$  ( $m/z$  15, IE = 9.84 eV<sup>50</sup>),  $\text{H}_3\text{CCH}$  ( $m/z$  28, IE = 8.3 eV, M06) or  $\text{H}_2\text{CCH}_2$  ( $m/z$  28, IE = 10.51 eV<sup>50</sup>),  $\text{C}_2\text{H}_5$  ( $m/z$  29, IE = 8.1 eV<sup>43</sup>), and  $\text{H}_2\text{COH}$  ( $m/z$  31 IE = 7.56 eV<sup>55</sup>).  $M/z$  44 is formed upon the pyrolysis of  $\text{HOCH}_2\text{CH}_3$  to  $\text{O}=\text{CHCH}_3 + \text{H}_2$ .  $M/z$  43 could be due to the dissociative photoionization:  $\text{O}=\text{CHCH}_3 + h\nu \rightarrow \text{C}_2\text{H}_3\text{O}^+ + \text{H}$ , with an appearance energy of  $10.50 \pm 0.05$  eV.<sup>56</sup>

#### 4.2. Effusive Beam, Tunable VUV-PI-TOFMS of HEHN.

The first tunable VUV-PI-TOFMS experiment on HEHN,  $[\text{HOCH}_2\text{CH}_2\text{NH}_2\text{NH}_2^+][\text{NO}_3^-]$ , utilized an effusive source for the ionic liquid sample, where the ionic liquid is placed in a temperature-controlled glass sample container.<sup>33</sup> The vapors given off of the heated sample penetrate through a pinhole into the photoionization region, and the product photoion masses are recorded as a function of sample temperature and photoionization energy (8.0–15.0 eV). The resulting photoionization efficiency (PIE) curves measure the photoion current as a function of photon energy and can be used to determine the ionization energy (IE) of parent photoions and appearance energies (AEs) of dissociative photoionization fragments with an estimated uncertainty of less than  $\pm 0.2$  eV. From the heated ionic liquid sample, the vaporization of the ionic liquid (if any), its volatile impurities, and its thermal decomposition products are detected simultaneously, somewhat complicating interpretation of the mass spectra. It should be noted that the time scale for these condensed-phase decomposition reactions is on the order of minutes, which is significantly longer than the time scale of the aerosol experiments ( $\sim 10$   $\mu\text{s}$ ). This experiment only allows for the detection of stable, closed-shell decomposition products, and this will be discussed in detail later.

In Figure 3, mass spectra can be seen for the HEHN ionic liquid at 200 °C at 9.0 and 12.6 eV photoionization energies. The primary thermal decomposition product of the protic ionic liquid HEHN is the neutral 2-hydroxyethylhydrazine ( $\text{HOCH}_2\text{CH}_2\text{NHNH}_2$ , HEH,  $m/z$  76) formed via proton transfer from the cation ( $\text{HOCH}_2\text{CH}_2\text{NH}_2\text{NH}_2^+$ ) to the anion ( $\text{NO}_3^-$ ), and the major dissociative ionization fragment of  $\text{HEH}^+$  is  $m/z$  45<sup>45</sup> (similar to Figure 1). The  $\text{HNO}_3$  coproduct is detected at  $m/z$  63 ( $\text{HNO}_3^+$ , IE = 12.0 eV<sup>50</sup>) with a major dissociative ionization fragment at  $m/z$  46 ( $\text{NO}_2^+$ , AE = 12.0

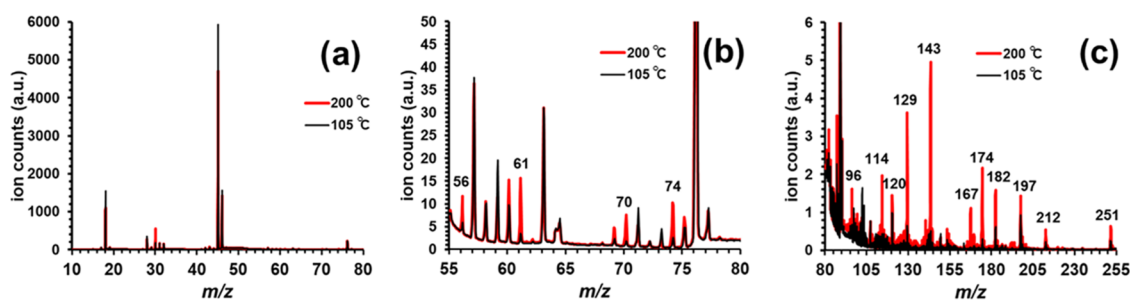


**Figure 4.** Total ion current VUV-PI mass spectra of HEHN from the VUV-PI-TOFMS effusive source (normalized to  $m/z$  76) at 105 °C (black) and 200 °C (red): (a) full scale, (b) enlarged spectra  $m/z$  55–80, and (c) enlarged spectra  $m/z$  80–255.

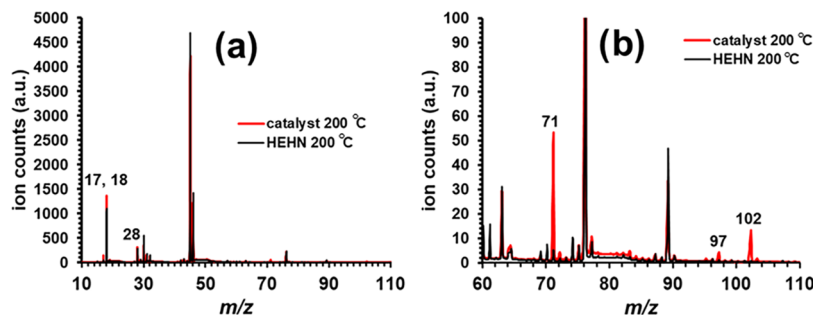
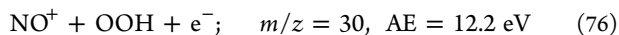
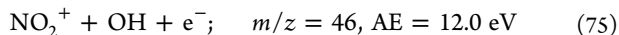
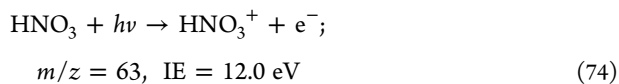
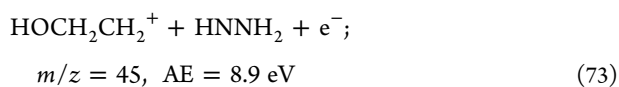
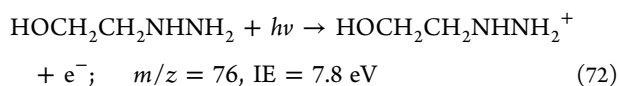
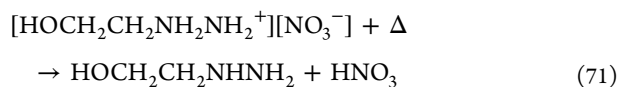


**Figure 5.** Total ion count VUV-PI mass spectra of HEHN from the VUV-PI-TOFMS effusive source (normalized to  $m/z$  76): (a) HEHN (black) and HEHN + Ir catalyst (red), source  $T = 200$  °C; and (b) enlarged spectra from panel (a).

$eV^{50}$ ) and a minor fragment at  $m/z$  30 ( $NO^+$ ,  $AE=12.2$  eV, M06/6-31(+)(d,p)):



Although HEH and  $HNO_3$  are produced in a 1:1 ratio via [reaction 71](#), the significant difference in relative total ion current (TIC) intensities of HEH versus  $HNO_3$  ([Figure 3](#)) could be due to the higher IE of  $HNO_3$ , its significant ion fragmentation to  $m/z$  46 via [reaction 75](#), and to a smaller photoionization cross section of  $HNO_3$  below 15 eV photon energies. It has been noted previously that the facile fragmentation of  $HNO_3^+$  must be considered in the interpretation of mass spectrometric data.<sup>6</sup>

To look for major decomposition products, it is informative to first generate the total ion current (TIC) mass spectrum, defined here as the sum of all mass spectra over all photon energies for a given temperature. In this way, significant differences in ion currents between various experimental conditions can be observed. For example, in [Figure 4](#), the

TIC mass spectrum at 105 °C is compared to that at 200 °C (normalized to the 105 °C HEH  $m/z$  76 peak). Besides the formation of HEH and  $HNO_3$ , the major difference in the TIC mass spectra between 105 and 200 °C is the formation of  $m/z$  30 with an experimental IE =  $9.1 \pm 0.2$  eV and smaller peaks are also observed (with IEs) at  $m/z$  56 (8.8), 60 (9.8), 61 (8.8), 69 (9.0), 70 (8.8), 74 (9.0), 96 (9.8), 114 (8.8), 120 ( $\sim 7.8$ ), 129 (9.0), 143 (9.2), 167 (9.4), 174 ( $< 8.0$  ( $\sim 7.0$ )), 182 (11.6), 197 (9.2), 212 (11.0), and 251 (11.2). The  $m/z$  30 peak cannot be  $H_2CO$  (IE = 10.8 eV)<sup>50</sup> as has been previously proposed as a thermal decomposition product of HEH<sup>42</sup> or  $C_2H_6$  (IE = 11.5 eV)<sup>50</sup> but can be assigned to the formation of  $NO$  (IE = 9.26 eV).<sup>50</sup> Although an  $m/z$  30  $NO^+$  fragment is possible from the dissociative ionization of  $HNO_3$ , via [reaction 76](#), it would need an appearance energy of greater than the IE of  $HNO_3$  of 12.0 eV, where the calculated appearance energy  $AE(NO^+) = 12.2$  eV (M06/6-31+G(d,p)). The possible mechanism for the formation of  $NO$  from the thermal decomposition of HEHN is unclear, and this will be addressed in a future publication.

In the previous work, the evolution of ethanolamine ( $HOCH_2CH_2NH_2$ , IE = 8.9 eV,<sup>50</sup>  $m/z$  61) as a decomposition product from HEH<sup>42</sup> and HEHN<sup>20</sup> has been proposed. The experimental IE of  $m/z$  61 of 8.8 eV matches the literature value well, and  $m/z$  61 is identified to be from ethanolamine, likely produced here by the heterogeneous dissociation of the N–N bond in HEH to produce ethanolamine and  $NH_3$ , and the catalytic  $NH_3$  production is discussed below. The IE/AEs of  $m/z$  56 and 60, at 8.8 and 9.8 eV, respectively, could indicate the photofragmentation of the ethanolamine cation ( $m/z$  61). Ethanolamine also exhibits a significant dissociative ionization fragmentation channel to produce  $CH_4N^+$  with an AE of 9.5 eV that could also contribute to the formation of  $m/z$  30. (Note, since we do not see ethanolamine formation in homogeneous pyrolysis of HEH during flash pyrolysis,  $m/z$  30

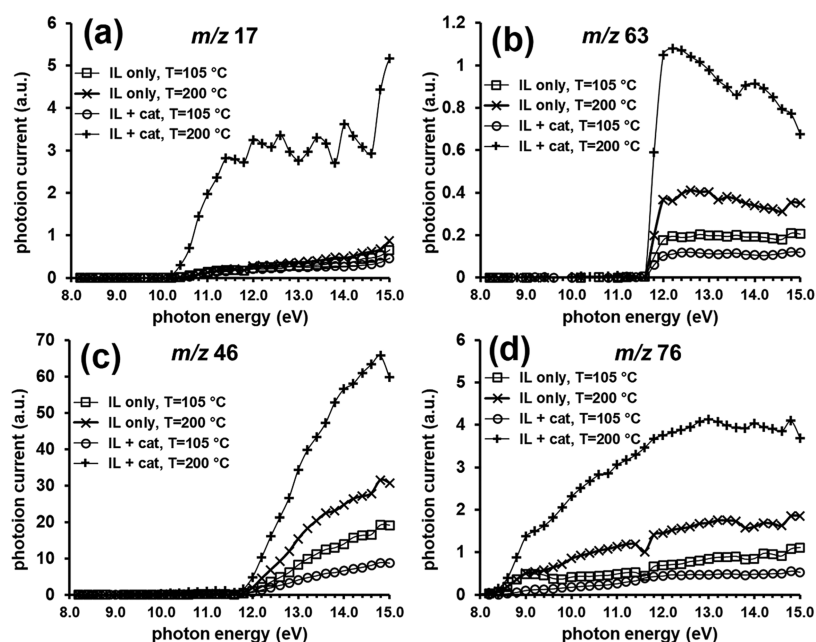


**Figure 6.** VUV-PI-TOFMS photoionization efficiency (PIE) curves from  $m/z$  17 (a), 63 (b), 46 (c), and 76 (d) photoions measured with HEHN and HEHN + Ir catalyst in the effusive source at source temperatures 105 and 200 °C.

was also absent there.) Observation of peaks at  $m/z$  69, 70, and 74, with IE/AEs of 9.0, 8.8, and 9.0 eV respectively, could be a result of subsequent fragmentation of  $\text{HEH}^+$  ( $m/z$  76,  $\text{HOCH}_2\text{CH}_2\text{NHNH}_2$ , IE = 7.8 eV) having in excess of 1.0 eV internal energy, although these peaks are not observed in the electron-impact ionization mass spectrum of HEH.<sup>45</sup> They could also be a result of dissociative photoionization of heavier products (effusing from the source) observed in Figure 4 or the dehydrogenation of HEH, although the loss of six or seven hydrogens to form  $m/z$  70 and 69, respectively, is unlikely. The other thermal decomposition peaks in Figure 4 that are above  $m/z$  77 will be compared to observations in the other techniques and will be discussed in Section 4.7.

The introduction of a small amount of iridium catalyst into the HEHN in the effusive source at 200 °C results in the significant increase in photoions of  $m/z$  17, 18, and 28 (Figure 5) and the formation of photoions not seen in significant quantities in the thermal decomposition products of HEHN (Figure 4), namely,  $m/z$  71, 97, and 102. The IE and/or AE of these photoions can be found in Table S1 in the SI. Possible identities of these photoions will be discussed briefly here and in more detail in comparison to the aerosol VUV-PI-TOFMS, NAIMS, and LDIDD-MS results below.

A significant benefit of tunable VUV-PI-TOFMS is that the PIE curves that are generated can be used to determine the IE of parent photoions and AE of dissociative photoionization fragments. PIE curves for  $m/z$  17, 63, 46, and 76 photoions can be seen in Figure 6. The experimental IE for  $m/z$  17 of  $10.0 \pm 0.2$  eV matches very well with the literature IE for  $\text{NH}_3$  (10.05 eV),<sup>50,57</sup> and the shape of the PIE curve is nearly identical to the literature data,<sup>57</sup> and so the  $m/z$  17 product is identified as  $\text{NH}_3$  with a high degree of confidence. Similarly, the literature IE for  $\text{HNO}_3$  is 12.0 eV<sup>50</sup> with an AE for  $m/z$  46 ( $\text{NO}_2^+$  fragment from  $\text{HNO}_3^+$ , reaction 75) of essentially the same energy, 12.0 eV,<sup>50</sup> and are a good match to both the experimental IE of  $m/z$  63 (11.8  $\pm$  0.2 eV) and the AE of  $m/z$  46 (11.8  $\pm$  0.2 eV). For HEH ( $m/z$  76), both the literature IE (7.6 eV)<sup>50</sup> and the M06/6-31+G(d,p) calculated IE (7.55  $\pm$

0.2 eV) values match very well with the experimental IE (7.8  $\pm$  0.2 eV).  $M/z$  18 is a good match for  $\text{H}_2\text{O}$  (literature IE = 12.621 eV)<sup>50</sup> with an experimental IE of  $12.4 \pm 0.2$  eV. The detection of the enhanced signal of  $m/z$  28 (IE = 10.4 eV) cannot be a result from photoionization of  $\text{N}_2$ , CO,  $\text{H}_2\text{CN}^*$ , or  $\text{HCNH}^*$  products, as their IEs are 15.58, 14.014, 9.4, and 7.3 eV, respectively.<sup>50</sup> The time scale for this experiment is likely too long to observe the possible production of  $\text{H}_2\text{CN}^*$  or  $\text{HCNH}^*$ , as they would react to form closed-shell species in the liquid. The likely identity of  $m/z$  28 is  $\text{C}_2\text{H}_4$ , with an IE 10.5 eV, which was also proposed in the flash pyrolysis of HEH above. However, we cannot rule out the possibility that  $m/z$  28 results from dissociative photofragmentation of the heavier species ( $m/z$  71, 97, and 102) being formed upon iridium addition to HEHN.

In comparing the PIE intensities for the species in Figure 6, it is apparent from the PIE signals for  $m/z$  63, 46, and 76 that not only does thermal decomposition produce  $\text{HNO}_3$  + HEH products—as evidenced by the increase in PIE signals from 105 to 200 °C—but also that the addition of the Ir catalyst into the effusive source with the HEHN enhances the evolution of HEH and  $\text{HNO}_3$  relative to HEHN thermal decomposition alone. This indicates that there is possibly a competition between thermal and catalytic routes to form HEH +  $\text{HNO}_3$ . In contrast, when evaluating the  $m/z$  17  $\text{NH}_3$  PIE signals in Figure 6, there is very little difference in the PIE signals from 105 to 200 °C for HEHN only, whereas there is a large enhancement (5 $\times$ ) in signal upon the introduction of the Ir catalyst at 200 °C, indicating the near-exclusive formation of  $\text{NH}_3$  via heterogeneous catalysis. To quantify product enhancement due to the catalytic effect, by comparing the total ion currents for thermal versus catalytic decomposition as a function of temperature (Figure S3), it is observed that a significant enhancement ( $\sim$ 3–10 $\times$ ) of  $m/z$  17, 71, 97, and 102 occurs when the Ir catalyst granule is introduced at 200 °C, whereas only a modest enhancement ( $\sim$ 2 $\times$ ) occurs for  $m/z$  18, 28, 30, 63, and 76. The possible identities of the  $m/z$  71, 97, and 102 species will be discussed in detail in Section 4.4.

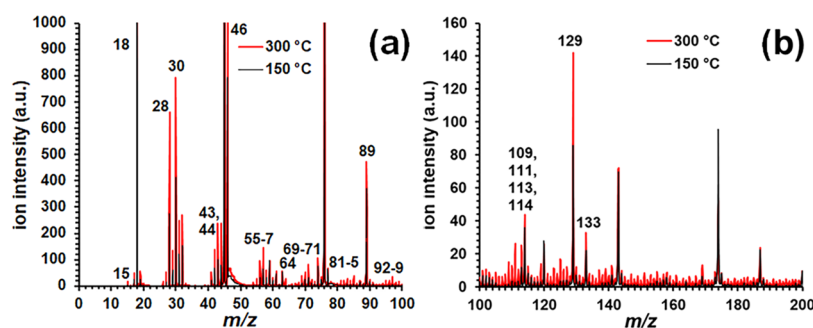


**Figure 7.** TIC mass spectra of the thermal decomposition of HEHN on copper at 150 °C (black) and 300 °C (red) (a) from  $m/z$  0 to 100 and (b) from  $m/z$  100 to 200.

### 4.3. Aerosol Beam, Tunable VUV-PI-TOFMS of HEHN.

The next set of experiments on HEHN were performed using aerosol tunable VUV-PI-TOFMS with either heated copper (noncatalytic) or iridium catalyst as targets for HEHN aerosols ( $T \leq 300$  °C).

**4.3.1. Thermal Decomposition of HEHN Aerosols on Copper.** In Figure 7, the total ion currents of HEHN aerosols on copper as a function of temperature (normalized to  $m/z$  76) show significant increases in  $m/z$  18, 28, and 30 between 150 and 300 °C. Smaller ion current increases were also observed for  $m/z$  43, 44, 46, 55–57, 64, 69–71, 81–85, 89, 92–99, 109–114, 129, and 133, and a small new peak appears at  $m/z$  15. Relative percent intensity values (%) and IE/AEs for all of these photoion peaks are listed in Table S2. A more detailed look at the PIE curves for the photoions produced as a function of temperature indicates that  $N_2O$  ( $m/z$  44) formation is possible at 300 °C (Figure 8).<sup>7</sup> Decreases in

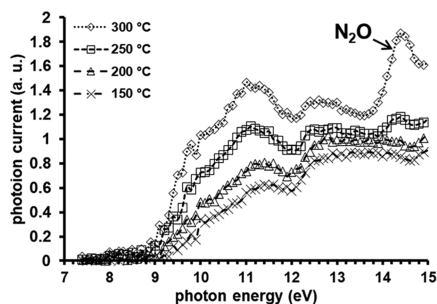


**Figure 8.** PIE curves of  $m/z$  44 from HEHN on copper at 150–300 °C. Note the increase in signal at  $T = 300$  °C between 14 and 15 eV, indicating the formation of  $N_2O$ .<sup>7</sup>

$m/z$  63 and 76 TIC mass spectral signals as the temperature increases above 200 °C (Figure S4) could indicate either the reduced formation of HEH and  $HNO_3$  with increasing temperature, lower signal due to the lower density of the hotter gases evolving from the copper surface, or, most likely, the thermal decomposition of  $HNO_3$  and HEH via secondary reactions, as evidenced by the increase in peaks with  $m/z < 76$  at 300 °C in Figure 7a. It should be noted that  $HNO_3$  has been previously observed to thermally decompose at  $T \geq 250$  °C to form  $NO_2$  under similar experimental conditions.<sup>6</sup> Possible identities of the remaining peaks seen in the thermal decomposition of HEHN aerosols on copper will be discussed in Section 4.4.

**4.3.2. Catalytic Decomposition of HEHN Aerosols on Iridium.** Upon the introduction of an iridium catalyst target in the ATOFMS, the total ion current mass spectral (normalized

to  $m/z$  76) comparison of the thermal decomposition of HEHN on copper at 300 °C with HEHN on an iridium catalyst target at 300 °C can be seen in Figure 9a,b. HEHN on the hot catalyst target displays an increase in all photoions that were observed in the thermal decomposition TIC mass spectrum (Figure 7) plus new peaks at  $m/z$  36, 38, 39, and 87 (Table S3). The increase in peaks can be attributed to possible catalytic enhancement of the proton transfer in reaction 1, thereby increasing the formation of HEH and  $HNO_3$ . The small  $m/z$  peaks at 36 and 38 (IE =  $12.5 \pm 0.2$  eV) found only upon the introduction of the Ir catalyst can be attributed to HCl (IE =  $12.744 \pm 0.009$  eV<sup>45</sup>) formed by the Ir surface reaction of  $HNO_3$  with  $Cl^-$  impurities in the ionic liquid, and the isotopic ratio of  $^{35}Cl/^{37}Cl \sim 3:1$  matches well with the intensity ratio of  $m/z$  36:38 in Figure 9b. The peak forming at  $m/z$  39 indicates the formation of a  $C_3H_3$  species, and this will be discussed in more detail in Section 4.4.1. The appearance of  $m/z$  87 could result from  $H_2$  loss from  $m/z$  89, and dehydrogenation reactions are also observed in the catalytic decomposition of HEH aerosols, discussed below.

The comparison of HEHN on an iridium catalyst target at 150 and 300 °C is shown in Figure 9c (full scale),d (magnified 10 $\times$ ). Increases in peaks at 300 °C occur at  $m/z$  15, 17, 18, 28, 30, 43, 44, 45, 55, and 56, and a new peak appears at  $m/z$  39. Upon further analysis of the PIE curves for each photoion, new features due to the introduction of the iridium catalyst granule are observed ( $m/z$  39 and 44; Figure 10). Again, the significant increase in the  $m/z$  39 signal (Figure 10a) could indicate the formation of a  $C_3H_3$  species, and this will be discussed in more detail below. While a small amount of  $N_2O$  ( $m/z$  44) was observed for thermal decomposition of HEHN on copper at 300 °C (Figure 8),  $N_2O$  production is detected at as low as 150 °C upon introduction of the iridium catalyst, indicated by the peak in the  $m/z$  44 PIE at 14.2 eV (Figure 10b). The mechanism for the formation of  $N_2O$  from HEHN must be somewhat complex, and understanding how  $N_2O$  is formed could play a critical role in the catalytic ignition of HEHN-based monopropellants, as has been noted previously in other ionic liquid ignition mechanisms.<sup>11,58</sup> An increase in  $m/z$  15 upon the introduction of the iridium catalyst granule can partially be attributed to the possible formation of  $CH_3^+$  due to dissociative photoionization of catalytic products with higher masses above 14.0 eV. However, the possible formation of  $\bullet CH_3$  radical was observed both in thermal decomposition at 300 °C and on the Ir catalyst target above 250 °C, both detected at IE =  $9.6 \pm 0.3$  eV, and this IE matches reasonably well with the literature IE of  $\bullet CH_3$  of  $9.837 \pm 0.005$  eV.<sup>50</sup> The formation and detection of  $\bullet CH_3$  were also seen in the flash

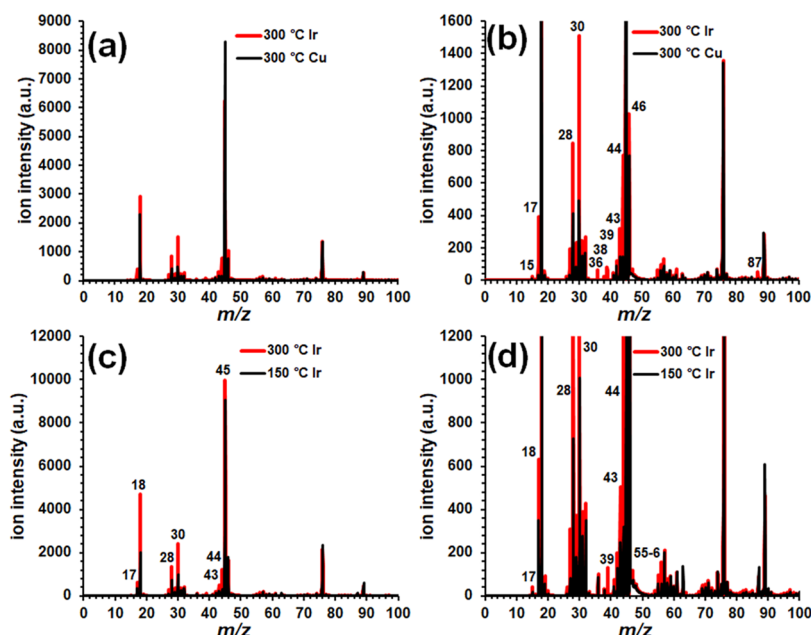


**Figure 9.** TIC mass spectra of HEHN on copper (black) and iridium catalyst (red) at 300 °C: (a) full scale and (b) magnified. TIC mass spectra of HEHN on iridium catalyst at 150 °C (black) and 300 °C (red): (c) full scale and (d) magnified. TIC mass spectral signals are normalized to  $m/z$  76.

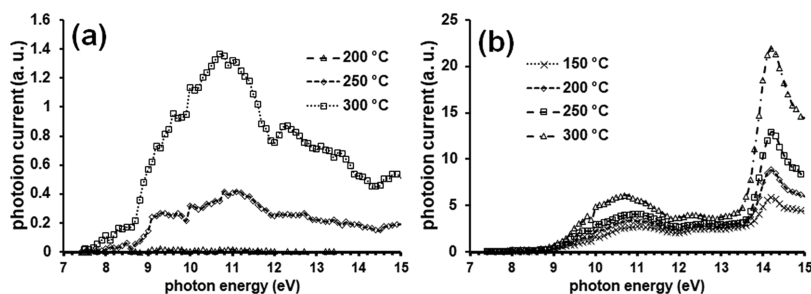


**Figure 10.** PIE curves of the catalytic decomposition of HEHN aerosols on an iridium catalyst as a function of temperature for (a)  $m/z$  39 and (b)  $m/z$  44 at a 0.1 eV photon energy resolution.  $m/z$  39 could indicate the formation of a  $C_3H_3$  species, and the  $m/z$  44 peak at 14.2 eV indicates the formation of  $N_2O$ .

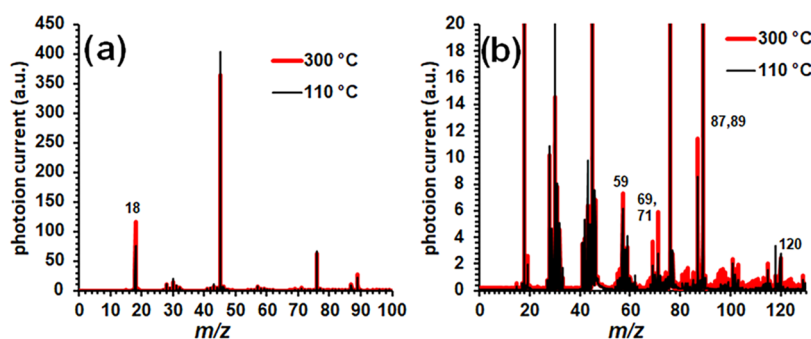


**Figure 11.** Normalized ( $m/z = 76$ ) total ion current mass spectra for HEH aerosol on copper from 7.4 to 15 eV at 110 °C (black) and 300 °C (red): (a) full scale and (b) magnified.

pyrolysis of HEH (Figure 1), and  $CH_3$  may be one contributor to the formation of the  $C_3H_3$  ( $m/z$  39) species mentioned above, and this is discussed further below.

#### 4.4. Aerosol Beam, Tunable VUV-PI-TOFMS of HEH.

As has been established above, the primary thermal decomposition products of HEHN are  $HNO_3$  and HEH neutrals formed upon proton transfer from the  $HOCH_2CH_2NH_2NH_2^+$  cation to the  $NO_3^-$  anion. In a

separate experiment, 2-hydroxyethylhydrazine (HEH—the neutral precursor to HEHN) aerosols were formed and introduced into the aerosol mass spectrometer at the ALS Beamline 9.0.2, with either a heated copper surface or a heated Ir catalyst as the aerosol target.

**4.4.1. Thermal Decomposition of HEH Aerosols on Copper.** Due to the relatively low enthalpy of vaporization for HEH,  $\Delta H_{vap} = 52.3 \pm 6.3$  kJ/mol (determined by

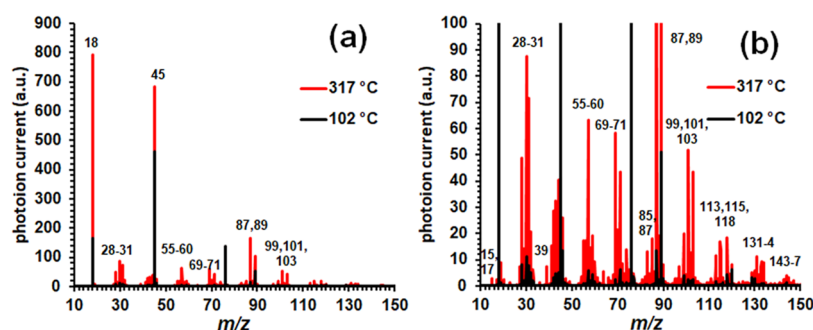


**Figure 12.** Normalized ( $m/z$  76) total ion current mass spectra of HEH aerosols on iridium catalyst at 102 °C (black) and 317 °C (red): (a) full scale and (b) magnified.

isothermal TGA<sup>8</sup>), HEH aerosol formation and introduction into the mass spectrometer were rather difficult, caused by the volatility of HEH. However, it was possible to introduce HEH aerosol particles into the aerosol mass spectrometer to a measurable extent by bypassing the drying tube. Mass spectra were recorded from 7.4 to 15 eV photoionization energy at heater block temperature of up to 300 °C. Total ion current mass spectra (normalized to  $m/z$  76) for HEH on the copper heater block at 110 °C (black traces) and 300 °C (red traces) can be seen in Figure 11. Increases in mass peaks are observed at  $m/z$  18, 59, 69, 71, 87, and 89. Experimental IE/AEs of peaks in Figure 11 are reported in Table S4.

**4.4.2. Thermal Decomposition of HEH Aerosols on Iridium.** Total ion current mass spectra (normalized to  $m/z$  76) for HEH on the iridium catalyst at 102 °C (black traces) and 317 °C (red traces) can be seen in Figure 12, and experimental IE/AEs of peaks in Figure 12 are reported in Table S5. It should be noted that, upon inspection of the  $m/z$  44 PIE curves, N<sub>2</sub>O was detected from HEH on iridium at 317 °C, indicating that the formation of N<sub>2</sub>O does not necessarily require the presence of NO<sub>3</sub><sup>-</sup> or HNO<sub>3</sub> to occur, and yet the N<sub>2</sub>O formation is more facile with HEHN (Figures 8 and 10b). An unavoidable impurity in the 2-hydroxyethylhydrazine (HEH) used to synthesize HEHN was previously identified by gas chromatography/mass spectrometry (GC/MS) as bis-hydroxyethylhydrazine (HOCH<sub>2</sub>CH<sub>2</sub>)<sub>2</sub>N<sub>2</sub>H<sub>2</sub>, with  $m/z$  120 (IE = 7.0 eV, M06/6-31+G(d,p)). This species exhibits significant fragment ions at 118, 89 (AE = 8.1 eV), 87, 71, and 69, and these peaks are also detected in this experiment and are attributed, at least in part, to bis-hydroxyethylhydrazine increases in the  $m/z$  87 to  $m/z$  89 and  $m/z$  69 to  $m/z$  71 peak ratios by 4 and 2 times, respectively, which indicates the enhancement of dehydrogenation reactions in the presence of an iridium catalyst. The catalytic dehydrogenation of bis-HEH to form  $m/z$  118 could indicate that the two hydroxyethyl functional groups are bonded to neighboring N atoms and H<sub>2</sub> loss forms an N=N double bond in the  $m/z$  118 product, whereas H<sub>2</sub> loss from a terminal NH<sub>2</sub> group is not energetically favorable. More discussion on the possible bis-HEH structures is explained below. The increase in mass peaks with molecular masses that are higher than HEH indicates that heterogeneous recombinations on the iridium surface, such as the addition of a second hydroxyethyl group to HEH to form bis-HEH, as well as the addition of •CH<sub>3</sub> to a C<sub>2</sub> species to form C<sub>3</sub>H<sub>3</sub>, are possible. The implication here is that on the catalyst surface, radical formation could play important roles as initiators and propagators in the ignition and combustion of HEHN-based monopropellants.

As mentioned previously with the HEHN aerosol catalytic decomposition results (Figure 10), a significant new product that was also observed in the HEH aerosol experiment but was not present in the HEHN effusive source experiment is the appearance of photoion  $m/z$  39 above  $T = 300$  °C. The experimental IE of 8.7 eV matches well with the literature value of 8.67 eV for propargyl radical (C<sub>3</sub>H<sub>3</sub>•)<sup>59</sup> and is significantly different from the literature IE for the alternative  $m/z$  39 cyclopropenyl radical (IE = 6.6 eV).<sup>50</sup> Additionally, the experimental PIE curve for  $m/z$  39 matches reasonably well with literature PIE curves<sup>59</sup> found for the propargyl radical (see Figure 13), and  $m/z$  39 is identified here with a reasonable level of certainty as the propargyl radical. The formation of propargyl radical in this catalytic system is significant in that HEH consists of a hydroxyethyl (C<sub>2</sub>) moiety, and the presence of the iridium catalyst likely plays an important and perhaps necessary role in the transformation of a C<sub>2</sub> to a C<sub>3</sub> species, possibly in reacting with a •CH<sub>3</sub> species formed as mentioned earlier. Additional theoretical work is required to address this finding.

**4.5. Comparison of the Two VUV-PI Methods.** There are several important differences in the effusive versus aerosol experiments to consider when analyzing the data: (1) the HEHN in the effusive source first must undergo decomposition (thermal and/or catalytic) to form HEH + HNO<sub>3</sub>, and HNO<sub>3</sub> is not present in the HEH aerosol experiment; (2) the effective reaction time for the effusive source is on the order of minutes, whereas for the aerosol source, the residence time of HEH on the catalyst is likely tens of microseconds<sup>6</sup> as the products are flash-vaporized from the hot catalyst surface into vacuum; and (3) the higher temperature of the aerosol experiment (300 versus 200 °C) could provide sufficient (thermal) energy for the HEH to react via pathways that are inaccessible in the lower-temperature effusive source. It should also be noted that the rapid vaporization into a high vacuum in the aerosol source could potentially minimize collisions (i.e., radical–radical recombinations) and allow for the detection of highly reactive radical species such as •CH<sub>3</sub> and •C<sub>3</sub>H<sub>3</sub> discussed previously.

**4.6. Nanotip Ambient Ionization Mass Spectrometry.** Nanotip ambient ionization mass spectrometry (NAIMS)<sup>14</sup> provides an alternate method to investigate the catalytic reactivity of HEHN on iridium. We employed two ambient ionization mass spectrometric techniques, including NAIMS and LDIDD-MS, which do not require a high vacuum for the reaction, and therefore provide a more realistic environment for the reaction of HEHN in the presence of Ir catalyst. Previous attempts to investigate this reactivity using another

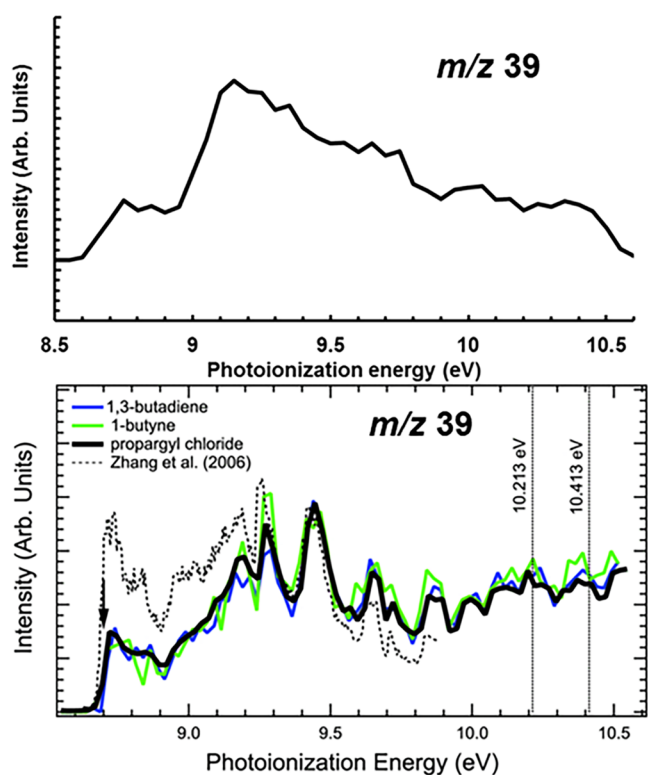


**Figure 13.** PIE curve for  $m/z$  39 (top, 25 meV photon energy resolution) from HEH aerosol catalytically decomposed on an iridium catalyst at 317 °C compared to literature PIE curves (bottom) for propargyl radical ( $C_3H_3^+$ ,  $m/z$  39) produced from 193 nm photolysis of 1,3-butadiene (blue), 1-butyne (green), and propargyl chloride (solid black), where the black arrow indicates a propargyl IE of 8.67 eV. The photoionization cross section measured by Zhang et al.<sup>60</sup> is shown as a dashed black line. Reprinted from ref 59, with the permission of AIP Publishing.

atmospheric mass spectrometric technique—desorption electrospray ionization mass spectrometry (DESI-MS)<sup>61</sup>—found that the DESI-MS method had insufficient ionizing power to detect the reaction products, and the nanotip ionization method that provides a harder ionization was selected and is discussed here. NAIMS creates a localized plasma between the sample and the nanotip by applying a high DC voltage to the nanotip, and ionization takes place within the plasma. The plasma is considered to be a hard ionization technique, which enables the ionization of species that are difficult to be ionized with soft ionization techniques such as that by electrospray ionization (ESI), DESI-MS, or matrix-assisted laser desorption/ionization (MALDI). Because the plasma generated in the NAIMS creates rather harsh conditions for samples, it can cause fragmentations of molecular and ionic species within the plasma and possible ablation of clusters from the sample surface, making the resulting mass spectrum somewhat complex. Ionization using NAIMS can create cationic species primarily by  $H^+$  addition to neutral species (especially to amines) rather than by the removal of an electron that is typical in electron-impact ionization (EI) mass spectrometry. In these NAIMS experiments, investigation of HEHN catalytic reactivity measured the high-resolution mass spectra for HEHN on an iridium catalyst at room temperature and at 100 °C, and any new or enhanced peaks observed at 100 °C indicate catalytic reaction products. The high resolution afforded by the Orbitrap mass spectrometer allows for the

precise determination of molecular formulas of the catalytic products at 100 °C and of the HEHN species present at 30 °C. Additionally, we employed collision-induced dissociation (CID) to elucidate the structural information of selected ions via tandem mass spectrometric analysis.

Mass spectra for HEHN on an iridium catalyst at 30 and 100 °C are presented in Figure 14, from which predicted molecular

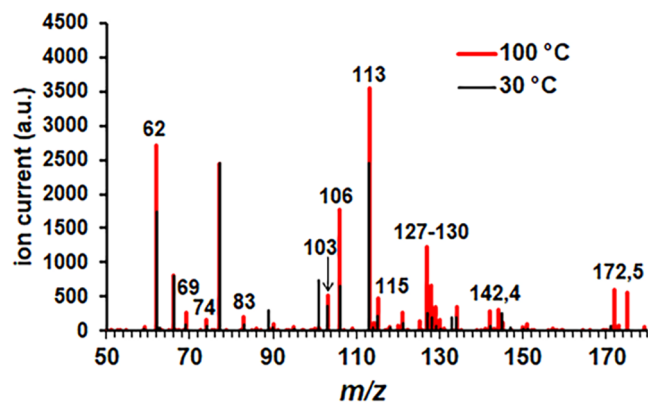


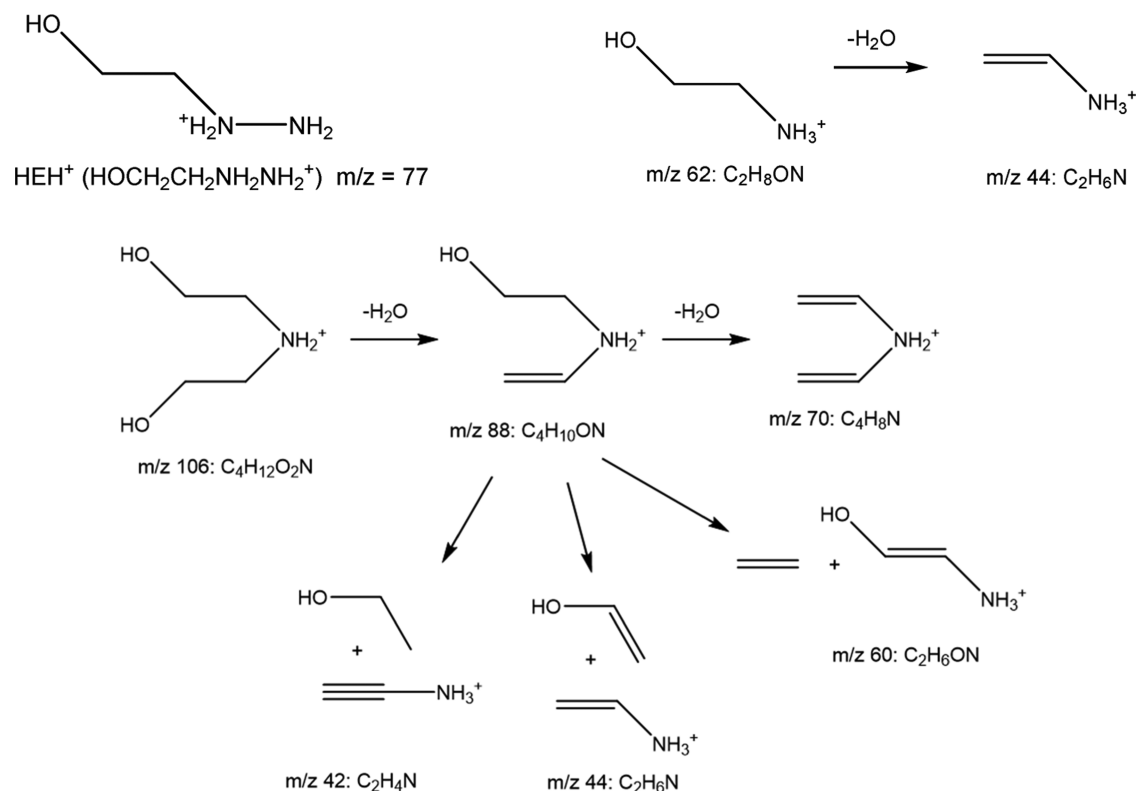
**Figure 14.** NAIMS spectra for HEHN on an iridium catalyst at 30 °C (black) and 100 °C (red) from  $m/z$  50 to 180.

formulas of specific masses observed by high-resolution NAIMS are listed in Table S6. CID fragmentation and detection of the fragment masses of specific products are also listed as primary ( $1^\circ$ ) and secondary ( $2^\circ$ ) fragments in Table S6. These fragmentation patterns give insight into the bonding structure of the parent ion. At a 100 °C iridium catalyst temperature, significant enhancement of mass peaks are observed at  $m/z$  62, 106, 113, 115, 127–130, 142, 144, 172, and 175, and signal enhancement to a lesser extent is observed for  $m/z$  69, 74, 83, 103, 121, 125, 130, and 134. Signal loss was observed for  $m/z$  89, 101, 133, and 145. Higher-mass peaks up to  $m/z$  500 were detected but, based on isotopic abundances, these peaks are believed to be products incorporating either iridium or tungsten from the catalyst surface or the nanotip, respectively, and are therefore excluded from this analysis.

The lowest mass product observed in Figure 14 is mass 62.0597, corresponding to the molecular formula  $C_2H_8ON$ . CID fragmentation and detection of the fragment masses from  $m/z$  62 indicate the loss of  $m/z$  18—a  $H_2O$  molecule, indicating a OH group in the  $m/z$  62 product. Based on the original structure of the hydroxyethylhydrazinium cation reactant,  $[HOCH_2CH_2NH_2NH_2]^+$ , along with its molecular formula  $C_2H_9ON_2$ , the product at  $m/z$  62,  $C_2H_8ON$ , has lost an HN ( $m/z$  15) and this leads to the proposed structure of  $m/z$  62 as  $HOCH_2CH_2NH_3^+$ , as seen in Scheme 1.

The structure of the observed peak at  $m/z$  106.0860 can be revealed by its molecular formula  $C_4H_{12}O_2N$  and its fragmentation pattern and structural similarity to  $HEH^+$ . The CID fragmentation of the  $m/z$  106 shows a primary loss of  $H_2O$  and a secondary loss of another  $H_2O$ , indicating the presence of two  $-OH$  groups in the  $m/z$  106 product. From subsequent CID of the primary  $m/z$  88 fragment, several fragmentation processes can occur: besides the second loss of a  $H_2O$  mentioned above, fragmentation can also eject an  $m/z$  28 ( $C_2H_4$ ) species or a 44 ( $C_2H_4O$ ) fragment, and at higher fragmentation energy, an  $m/z$  46 ( $C_2H_6O$ ) fragment also. The observed fragmentation processes are proposed in Scheme 1, yielding  $(HOCH_2CH_2)_2NH_2^+$  and indicating the loss of an

**Scheme 1.** CID Fragmentation Patterns and Possible Chemical Structures for Masses 62.05968 and 106.08604 Detected from NAIMS of HEHN on an Ir Catalyst at 100 °C



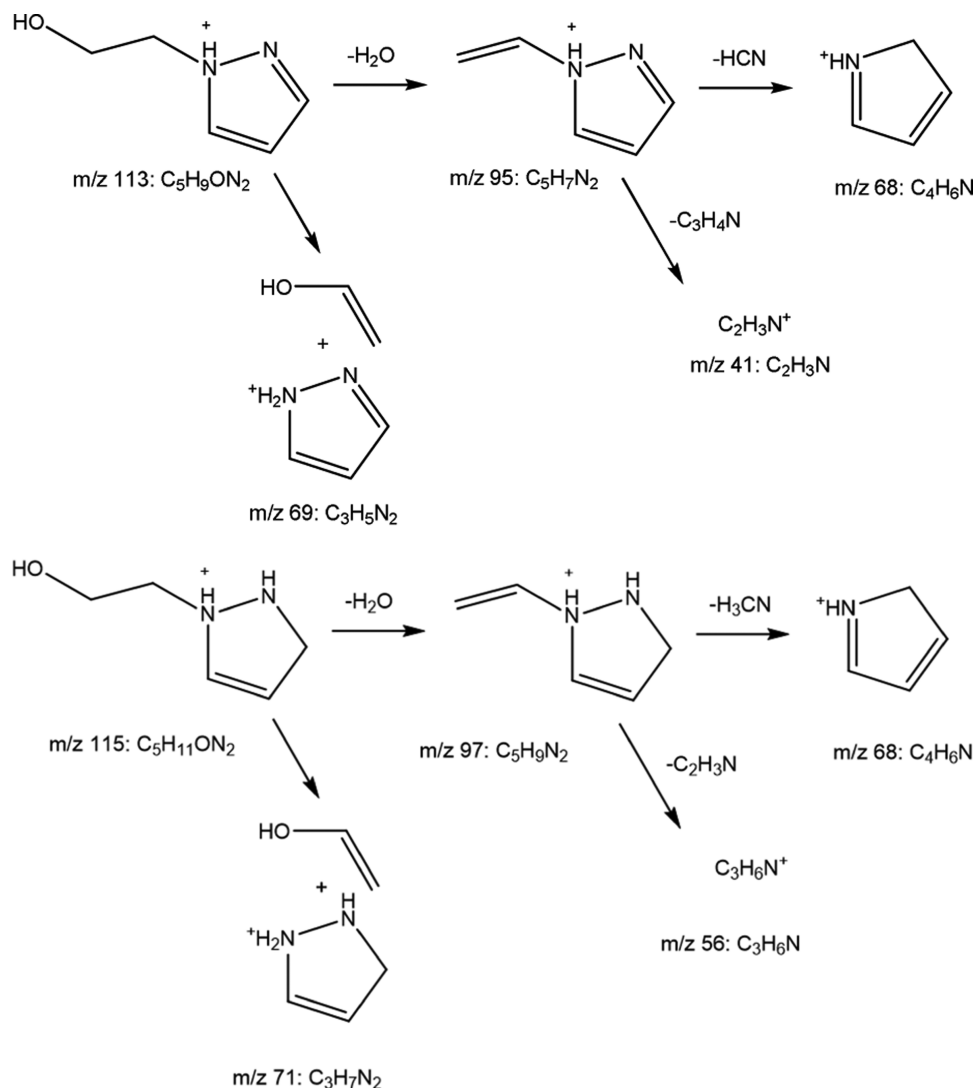
NH<sub>2</sub> group from one HEH and the addition of a second hydroxyethyl (HOCH<sub>2</sub>CH<sub>2</sub>) group to the same N atom on this species. This structure would indicate that the bis-HEH is also formed on the hot catalyst surface with both hydroxyethyl groups bonded to the same N atom (1,1-bis-HEH), in contrast to the previously mentioned bis-HEH structure (1,2-bis-HEH), in which the proposed catalytic dehydrogenation from neighboring N atoms occurs to form *m/z* 118.

As the product masses become larger, identifications of the catalytic products are more challenging. The products detected at *m/z* 113.0707 (C<sub>5</sub>H<sub>9</sub>ON<sub>2</sub>) and *m/z* 115.0864 (C<sub>5</sub>H<sub>11</sub>ON<sub>2</sub>) only differ by two hydrogens, potentially indicating the formation of a C=C or C=N bond in *m/z* 113.0707 versus a C-C or C-N bond in *m/z* 115.0864, and it is possible that they have very similar structures and formation mechanisms. The primary loss of H<sub>2</sub>O and *m/z* 44.0262, identified by high-resolution MS as C<sub>2</sub>H<sub>4</sub>O from both *m/z* 113.0707 and 115.0864, indicates the presence of a -OH group and a hydroxyethyl group in these products, respectively. Presumably, the H<sub>2</sub>O loss may arise from the hydroxyethyl group itself, indicating either the loss of H<sub>2</sub>O or C<sub>2</sub>H<sub>4</sub>O but not both (which would form a product fragment of, for example, 113.0707 - (18.0106 + 44.0262) = 51.0339, and *m/z* 51.0339 is not observed in the fragmentation of *m/z* 113.0707). While the secondary fragments of *m/z* 113.0707 and 115.0864 are different, one secondary fragmentation pathway of the primary fragments *m/z* 95 from 113.0707 and *m/z* 97 from 115.0864 both produce an *m/z* 68.0500 fragment (C<sub>4</sub>H<sub>6</sub>N). These common CID fragments could indicate that both species detected at *m/z* 113.0707 and 115.0864 share a common or similar structure with slightly different bond orders, such as an alkenyl versus an alkyl or imine versus amine moiety being

present. For example, the common *m/z* 68.0500 fragment C<sub>4</sub>H<sub>6</sub>N could be the 2*H*-pyrrolium cation (C<sub>4</sub>H<sub>6</sub>N<sup>+</sup>; Scheme 2). The primary fragment of H<sub>2</sub>O loss from *m/z* 113.0707, *m/z* 95.0609 (C<sub>5</sub>H<sub>7</sub>N<sub>2</sub>), could be the 1-ethenyl-1*H*-pyrrolium cation or the 1-ethenyl-1*H*-imidazolium cation. The primary fragment of H<sub>2</sub>O loss from *m/z* 115.0864, *m/z* 97.0766 (C<sub>5</sub>H<sub>9</sub>N<sub>2</sub>), could be the 1-ethenyl-4,5-dihydro-1*H*-pyrrolium cation or the 1-ethenyl-4,5-dihydro-1*H*-imidazolium cation. In Scheme 2, the CID fragmentation pathways of the proposed catalytic products 1-(2-hydroxyethyl)-1*H*-pyrazol-1-ium (*m/z* 113.0707) and 1-(2-hydroxyethyl)-2,3-dihydro-1*H*-pyrazol-1-ium (*m/z* 115.0864) are depicted.

To verify the fragmentation mechanisms depicted in Scheme 2, Born-Oppenheimer molecular dynamics (BOMD) simulations (Gaussian 16, PM6, 3000–5000 K, step size = 10 000) were carried out on the *m/z* 113, 95, and 97 species. Multiple trajectories confirmed the H<sub>2</sub>O loss (via hydroxyethyl C1H to OH transfer) from *m/z* 113.0707 to form *m/z* 95.0609, and *m/z* 95.0609 can fragment to *m/z* 68.0500 either by C<sub>2</sub>H<sub>3</sub> loss from the C-N bond cleavage or by HCN loss due to ring breaking. Similar processes were observed in the fragmentation of *m/z* 115.0864 in Scheme 2, and instead of HCN elimination, H<sub>2</sub>CNH was observed to be eliminated from the ring to form *m/z* 68.0500.

A useful tool to help determine the structures of these products is the degree of unsaturation (DOU), defined as the sum of double bonds, triple bonds, and the number of rings in the molecule.<sup>62</sup> Determination of the DOU for the corresponding neutral product molecules and their fragments are listed in Table S6. For *m/z* 113.0707 and 115.0864, having a DOU of 3 and 2, respectively, indicated the presence of multiple bonds and/or rings in the structure. The DOU values

Scheme 2. Proposed Structures of  $m/z$  113.0707 (Top) and  $m/z$  115.0864 (Bottom) HEHN Catalytic Decomposition Products and Their CID Fragmentation Pathways

for the fragmentation patterns indicated above are consistent with the proposed fragmentation mechanisms.

From Table S6, the molecular formula of  $m/z$  127.0864 is  $C_6H_{11}ON_2$  and  $m/z$  129.1020 is  $C_6H_{13}ON_2$ . Like  $m/z$  113.0707 and 115.0864, the products  $m/z$  127.0864 and 129.1020 only differ by two hydrogens, so their structures are assumed to be similar and the fragmentation patterns of these products could imply that both species can fragment by  $H_2O$  or  $C_2H_4O$  loss, indicating that the hydroxyethyl group is present/intact in these products. Two possible structures for  $m/z$  127.0864 and 129.1020 that are consistent with the fragmentation patterns and DOU values in Table S6 are presented in Scheme S1.

One product in the NAIMS experiments that is of interest due to its possible similar structure to the  $m/z$  102 product observed in the photoionization mass spectra earlier in this work (Figure 14) is  $m/z$  103.0864, which is identified here as  $C_4H_{11}ON_2$ . If this product, ionized by  $H^+$  addition producing an  $[M + H]^+$  ion, is similar to the  $m/z$  102 in the ALS experiments that is ionized by electron removal/photoionization to produce an  $M^+$  ion, the molecular formula for  $m/z$  102 in the ALS experiments would be  $C_4H_{10}ON_2$ . This

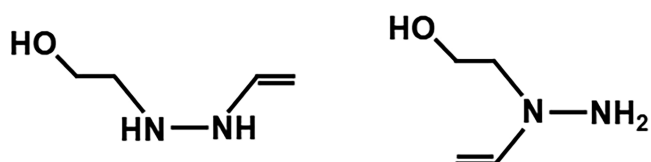
product could be a result of dehydration of one of the hydroxyethyl ( $HOCH_2CH_2-$ ) groups on *bis*-HEH ( $m/z$  120), resulting in a vinyl ( $H_2C=CH-$ ) group on the N–N backbone, with the possibility of having both the vinyl and the remaining hydroxyethyl functional groups on the same N atom ( $(HOCH_2CH_2)(H_2C=CH)NHNH_2$ ) or on neighboring N atoms ( $(HOCH_2CH_2)NHNH(CH=CH_2)$ ).

Primary fragmentation of the NAIMS  $m/z$  103.0864 product indicates the presence of a hydroxyethyl group (by  $18/H_2O$  and  $44/C_2H_4O$  loss discussed above), as well as  $C_2H_6O$  loss and  $C_2H_4$  loss to a lesser extent, and these fragments are consistent with the  $m/z$  102 species proposed above. Secondary fragmentation of the ( $m/z$  103.0864– $H_2O$ ) fragment  $m/z$  85.0758 indicates the loss of  $41/C_2H_3N$ ,  $28/C_2H_4$ ,  $55/C_3H_5N$ , and  $17/NH_3$ . Interestingly, the NAIMS fragmentation pattern of  $m/z$  103 can arise from the loss of  $NH_3$  from the  $m/z$  85.0758 primary fragment ( $C_4H_9N_2$ ) as a secondary fragmentation process, and this could indicate that both the hydroxyethyl and vinyl groups are on the same N atom, leading to facile  $NH_3$  elimination. However, it is also possible that both isomers are formed—if the hydroxyethyl and vinyl groups are located on neighboring N atoms, CID

would display fragmentation to either  $m/z$  42 and 43 or  $m/z$  41 and 44 species, and fragmentation of  $m/z$  85.0758 to  $m/z$  44 ( $-\text{C}_2\text{H}_3\text{N}$ ) is also observed. The two isomers have similar free energies of formation at 298 K ( $\Delta G_f^\ddagger$ ) within 11 kJ/mol (M06/6-31+G(d,p)), with the isomer having both of the functional groups on the same N being slightly favored. One possible  $m/z$  103.0864 structure and CID fragmentation pathway (with both of the functional groups on the same N) are depicted in Scheme S2 and consistent with the calculated DOU values in Table S6.

Ideally, the IEs of the two possible  $m/z$  103 isomers could help in identifying the isomers observed in the catalytic products. The experimental value of  $m/z$  102 with an IE =  $8.0 \pm 0.2$  eV and theoretical IEs (M06/6-31+G(d,p)) of two possible isomers of  $\text{C}_4\text{H}_{10}\text{ON}_2$ , having either the hydroxyethyl and vinyl on the same N ((HOCH<sub>2</sub>CH<sub>2</sub>)(H<sub>2</sub>C=CH)NNH<sub>2</sub>) or with each group on neighboring N atoms ((HOCH<sub>2</sub>CH<sub>2</sub>)-NHNH(CH=CH<sub>2</sub>)), are 7.2 (8.5 vertical) and 7.0 (8.4 vertical) eV, respectively (Scheme 3).

Scheme 3. Proposed  $m/z$  103 Isomers



The experimental IE of  $m/z$  102 (IE =  $8.0 \pm 0.2$  eV) does not match with the calculated adiabatic IEs but is closer to the calculated vertical IEs. This observation suggests that the Franck–Condon factor for the adiabatic photoionization is small at the adiabatic threshold due to large geometry changes between the neutrals and their corresponding cations. In any case, the theoretical IEs for the two isomers are nearly identical, and it would be difficult to distinguish with confidence the isomer(s) detected in this experiment. It should be noted that if both  $m/z$  103.0864 and 106.0860 are formed from bis-HEH ( $m/z$  120.1017), the former via elimination of a hydroxy group and the latter via NH<sub>3</sub> elimination, then the NH<sub>3</sub> elimination pathway (direct elimination to form  $m/z$  106.0860 and secondary fragmentation of the  $m/z$  85.0758 primary fragment from  $m/z$  103.0864) could support the formation of the bis-HEH isomer with the two hydroxyethyl groups on the same N atom. In the future, a more detailed theoretical analysis of this process will be necessary for determining the energetics involved in the heterogeneous formation of these isomers and for quantifying the branching ratios in these processes.

The remaining higher  $m/z$  peaks observed in the experiments, along with their molecular formulas and DOU values, are reported in Table S6. Identification of these products is more complicated and will be addressed in a future publication.

**4.7. Laser Desorption Ionization Droplet Delivery Mass Spectrometry.** Laser desorption ionization droplet delivery mass spectrometry (LDIDD-MS)<sup>15</sup> was the final method used to investigate the thermal and catalytic decomposition of HEHN. By comparing the mass spectra of HEHN on Teflon and on the iridium catalyst at 30 and 150 °C, the enhancement or appearance of mass peaks at 150 °C on iridium indicates the catalytic activity of HEHN on iridium, as seen in Figure 15. The only apparent difference in the mass spectra of HEHN on Teflon at 30 versus 150 °C was the growth of peaks at  $m/z$  106, 121, and 175. Upon introduction of the iridium catalyst, new peaks appear at 150 °C at  $m/z$  127, 129, 149, and 171, and significant enhancement of peaks is observed for  $m/z$  77, 103, 106, 121, and 175, with lesser enhancement of peaks observed at  $m/z$  59, 62, 70, 74, 87, 88, 96, 135, and 201. Mass peaks that are common for HEHN catalytic decomposition for both NAIMS and LDIDD-MS are listed in Table S7. The proposed identification of masses by high-resolution CID MS/MS is as follows:  $m/z$  59 is identified as H<sub>2</sub>C=CHNH<sub>2</sub>NH<sub>2</sub><sup>+</sup> (HEH - H<sub>2</sub>O),  $m/z$  85 as either pyrimidinium or methylpyrrolidinium,  $m/z$  62 as ethanolamine as described above, and the  $m/z$  > 100 peaks are identified as those described previously in the NAIMS section above.

**4.8. Comparison of Results from All of the Techniques.** This work presents a multimodal investigation of the thermal and catalytic decomposition mechanisms of HEHN. The first method, flash pyrolysis VUV-PI-TOFMS, yields information on the homogeneous, unimolecular thermal decomposition of HEH (the precursor/product of HEHN) and gives insight into the various pathways involved in gas-phase reactivity that can occur, including the detection and identification of radical species with short lifetimes. The tunable VUV-PI-TOFMS approach adds an additional dimension to the mass spectra, allowing the determination of not only the mass-to-charge ratios of the ions from the corresponding products but their photoionization energies and/or appearance energies as well. This enhanced technique can thus help to differentiate between species with the same mass-to-charge ratios but different IEs, such as N<sub>2</sub>O versus CO<sub>2</sub>. The power of the high-mass-resolution ambient ionization mass spectrometric techniques of NAIMS and LDIDD-MS additionally allows for the determination of the product molecular formulas with a high degree of certainty. Finally, the added benefit of collision-induced fragmentation of parent ions in NAIMS and LDIDD-MS further provides

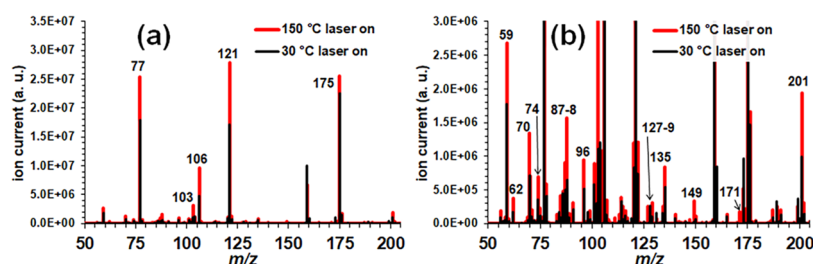


Figure 15. LDIDD-MS of HEHN on an iridium catalyst at 30 °C (black trace) and 150 °C (red trace), where panel (a) is full scale and panel (b) is magnified 10 $\times$ .

structural information about the parent ion, such as the possible nature of functional groups and the structural motifs. For example, the loss of  $m/z$  18 indicates the elimination of water, which could be the result of a 1,2H transfer to the O on a terminal OH group in  $\text{HEH}^+$  ( $m/z$  77), resulting in  $\text{H}_2\text{O}$  elimination, thereby indicating the presence of a OH functional group in the parent molecule.

When these complementary techniques are used together, the entire data set generated in this manuscript helps us to identify the thermal and catalytic products of HEHN by measuring (1) the mass-to-charge ratios of products, (2) the ionization energies of products or appearance energies of photofragments, (3) the molecular formulas, and thus their degrees of unsaturation, and (4) the fragmentation patterns of selected products. From this data, possible reaction product structures can be proposed. Energetic properties (thermodynamic stabilities, ionization energies, fragmentation energies, etc.) of the proposed products can then be calculated using quantum chemical ab initio methods to further elucidate the details of the possible structures.

Rather than attempt to identify all of the observed peaks in the mass spectra, we focused here on selected products that are commonly observed across different experiments and those products that are likely to give the most insight into the thermal and catalytic decomposition mechanisms. We have identified the HEH and HEHN thermal and catalytic decomposition products  $\bullet\text{CH}_3$  ( $m/z$  15),  $\text{NH}_3$  ( $m/z$  17),  $\text{H}_2\text{O}$  ( $m/z$  18),  $\text{C}_2\text{H}_4$  ( $m/z$  28),  $\text{H}_2\text{CNH}$  ( $m/z$  29),  $\text{NO}$  ( $m/z$  30),  $\text{N}_2\text{O}$  ( $m/z$  44),  $\text{HOCH}_2\text{CH}_2\text{NH}_2$  ( $m/z$  61),  $\text{HNO}_3$  ( $m/z$  63), and HEH ( $m/z$  76), as well as higher-mass products at  $m/z$  102 and 120 and at  $m/z$  103, 106, and 121 (VUV-PI-TOFMS and NAIMS/LDIDD, respectively). Possible structures of higher-mass products based on their high-resolution masses of  $m/z$  113, 115, 127, and 129 have also been proposed.

From the species identified above, there are several similarities that can give insight into the HEHN decomposition process. The identification of ammonia ( $\text{NH}_3$ ), ethanolamine ( $\text{HOCH}_2\text{CH}_2\text{NH}_2$ ,  $m/z$  61), and  $m/z$  106 ( $(\text{HOCH}_2\text{CH}_2)_2\text{NH}_2^+$ ) indicates that the N–N bond in HEH is readily broken on the iridium catalyst. The formation of  $m/z$  106 ( $(\text{HOCH}_2\text{CH}_2)_2\text{NH}_2^+$ ) could occur either directly by way of reaction of a hydroxyethyl with ethanolamine  $\text{HOCH}_2\text{CH}_2 + \text{HOCH}_2\text{CH}_2\text{NH}_2 \rightarrow (\text{HOCH}_2\text{CH}_2)_2\text{NH}$  or indirectly via deamination of 1,1-bis-HEH. Bis-HEH ( $m/z$  120) could form directly by the reaction of a hydroxyethyl with HEH, although it cannot be determined whether the second hydroxyethyl adds to the same or neighboring N atom as the hydroxyethyl in HEH. The formation of  $m/z$  102–103 ( $(\text{HOCH}_2\text{CH}_2)(\text{H}_2\text{C}=\text{CH})\text{N}_2\text{H}_2$ ) could occur by the  $\text{C}_2\text{H}_3$  addition to HEH, or, more likely, by dehydration of bis-HEH. Again, it is not clear if the hydroxyethyl and vinyl groups reside on the same or neighboring N atoms in this product. It is also possible that for both bis-HEH and  $m/z$  102, both isomers (1,1- and 1,2-) are formed. The higher-mass products detected in these experiments could possibly be formed by sequential addition, dehydration, deamination, and cyclization to species with  $m/z > 76$  (HEH).

In comparing the catalytic product masses observed using NAIMS and LDIDD-MS to those observed using VUV-PI-TOFMS, there are some interesting similarities. For example, from the ALS experiments, product photoions are observed at  $m/z$  102, 114, 120, 129, 143, and 174, while in the NAIMS

experiment, product ions are observed at 103, 115, 121, 130, 144, and 175, and in the LDIDD-MS experiment, product ions are also observed at 103, 121, and 175 that could potentially be similar to the products detected in the ALS experiments. Due to the differences in product ionization, reaction temperatures, and reaction pressures between the experimental techniques, the differences in the masses could be the result of (1) protonation ( $m/z + 1$ ) upon ionization from NAIMS, (2) dissociative photoionization from VUV-PI-TOFMS ( $m/z - 1$ ,  $m/z - 2$  for H or  $\text{H}_2$  elimination), or (3) high-temperature catalytic dehydrogenations ( $m/z - 2$ :  $\text{H}_2$  elimination). Dehydrogenation is likely responsible for the observation of  $m/z$  74 ( $\text{HEH-H}_2$ ), 118 (bis- $\text{HEH-H}_2$ ), and the dissociative photoions of bis-HEH/bis- $\text{HEH-H}_2$ , namely,  $m/z$  89/87 and 71/69.

Finally, the production of several species that are likely responsible for and significantly contribute to ignition and combustion of HEHN is  $\bullet\text{CH}_3$ ,  $\text{NO}$ ,  $\bullet\text{C}_3\text{H}_3$ , and  $\text{N}_2\text{O}$ . Methyl and propargyl radicals can facilitate and propagate further reactions by H-abstraction or addition to closed-shell species and are possibly responsible for the formation of products with an odd number of carbons such as  $m/z$  113 ( $\text{C}_3\text{H}_9\text{ON}_2^+$ ) and 172 ( $\text{C}_7\text{H}_{14}\text{O}_2\text{N}_3^+$ ). The formation mechanism of  $\text{NO}$  from HEHN is unclear at this point but could result from the  $\text{HNO}_3$  decomposition, and this will be addressed in a future publication.  $\text{NO}$  may easily convert to  $\text{NO}_2$ . The production of  $\text{N}_2\text{O}$ , an oxidizer/combustion accelerator, likely proceeds through a complex reaction mechanism, and the presence of the nitrate anion in HEHN is not required to produce  $\text{N}_2\text{O}$ , as it is also observed to evolve from HEH only on the hot catalyst.

## 5. CONCLUSIONS

This work describes the experimental work performed on the decomposition of HEHN and on 2-hydroxyethylhydrazine, the molecular precursor and primary thermal decomposition product of HEHN. Products observed experimentally and identified through DFT calculations and BOMD simulations are generally consistent with previous studies of HEH and HEHN. Herein, we have attempted to identify new chemical species from thermal and catalytic decomposition processes. Perhaps, of most significance are the observation of  $\bullet\text{CH}_3$  and propargyl radical ( $\bullet\text{C}_3\text{H}_3$ ) formation, and these species are believed to lead to recombination reactions resulting in products with higher masses than the original HEH reactant. Other reactions of significance are the heterogeneous dehydration and deamination reactions and possible vinyl or hydroxyethyl addition reactions. Finally, the formation and subsequent decomposition of ethanol upon homogeneous, unimolecular thermal decomposition of HEH may proceed through a nonstatistical, dynamic process. These products could be important in developing improved chemical kinetics models for catalytic ignition and combustion of HEHN-based monopropellants, and incorporation of these species into the kinetics models could result in improved fidelity for predictions of monopropellant thruster performance. Additional theoretical work, such as high-level ab initio, molecular dynamics, and phase space theory or Rice–Ramsperger–Kassel–Marcus (RRKM) kinetics calculations, is needed to understand HEH pyrolysis and to explain such observations as the transformation of  $\text{C}_2$  to  $\text{C}_3$  to form the propargyl radical and the formation of  $\text{N}_2\text{O}$  in the catalytic reaction of HEH on an iridium catalyst.

## ■ ASSOCIATED CONTENT

### SI Supporting Information

The Supporting Information is available free of charge at <https://pubs.acs.org/doi/10.1021/acs.jpca.1c07408>.

Relevant PES diagrams; additional experimental results on N<sub>2</sub>H<sub>2</sub> and HOCH<sub>2</sub>CH<sub>3</sub>; complementary tables and figures for VUV-PI-TOFMS results; additional high-resolution mass spectrometry data and fragmentation schemes; and molecular dynamics results (PDF)

## ■ AUTHOR INFORMATION

### Corresponding Author

Ghanshyam L. Vaghjiani – *In-Space Propulsion Branch, Rocket Propulsion Division, Air Force Research Laboratory, AFRL/RQRS, Edwards Air Force Base, California 93524, United States*; [orcid.org/0000-0001-7473-7388](https://orcid.org/0000-0001-7473-7388); Phone: 661-275-5657; Email: [ghsanshyam.vaghjiani@us.af.mil](mailto:ghsanshyam.vaghjiani@us.af.mil); Fax: 661-275-5471

### Authors

Steven D. Chambreau – *Jacobs Technology, Inc., Edwards Air Force Base, California 93524, United States*

Denisia M. Popolan-Vaida – *Department of Chemistry, University of California, Berkeley, California 94720, United States; Chemical Sciences Division, Lawrence Berkeley National Laboratory, Berkeley, California 94720, United States; Department of Chemistry, University of Central Florida, Orlando, Florida 32816, United States*

Oleg Kostko – *Chemical Sciences Division, Lawrence Berkeley National Laboratory, Berkeley, California 94720, United States*; [orcid.org/0000-0003-2068-4991](https://orcid.org/0000-0003-2068-4991)

Jae Kyoo Lee – *Department of Chemistry, Stanford University, Stanford, California 94305, United States*

Zhenpeng Zhou – *Department of Chemistry, Stanford University, Stanford, California 94305, United States*

Timothy A. Brown – *Department of Chemistry, Stanford University, Stanford, California 94305, United States*

Paul Jones – *Department of Chemistry, University of California, Riverside, California 92521, United States*

Kuanliang Shao – *Department of Chemistry, University of California, Riverside, California 92521, United States*

Jingsong Zhang – *Department of Chemistry, University of California, Riverside, California 92521, United States*; [orcid.org/0000-0003-3700-151X](https://orcid.org/0000-0003-3700-151X)

Richard N. Zare – *Department of Chemistry, Stanford University, Stanford, California 94305, United States*; [orcid.org/0000-0001-5266-4253](https://orcid.org/0000-0001-5266-4253)

Stephen R. Leone – *Departments of Chemistry and Physics, University of California, Berkeley, California 94720, United States; Chemical Sciences Division, Lawrence Berkeley National Laboratory, Berkeley, California 94720, United States*; [orcid.org/0000-0003-1819-1338](https://orcid.org/0000-0003-1819-1338)

Complete contact information is available at: <https://pubs.acs.org/doi/10.1021/acs.jpca.1c07408>

### Notes

The authors declare no competing financial interest.

## ■ ACKNOWLEDGMENTS

This material was based upon work supported by the Air Force Office of Scientific Research under award numbers FA9300-20-F-9801 (S.D.C. and G.L.V.), FA9550-10-1-0163, FA9550-14-

0154, and FA9550-19-1-0314 (S.R.L.), and FA9550-12-1-0400 and FA9550-16-1-0113 (J.K.L., Z.Z., T.B., and R.N.Z.). The work at the ALS was supported by the Director, Office of Energy Research, Office of Basic Energy Sciences, Chemical Sciences Division of the U.S. Department of Energy under Contract No. DE-AC02-05CH11231 (D.M.P.-V., O.K., and S.R.L.). This research used resources of the Advanced Light Source, a U.S. DOE Office of Science User Facility under contract no. DE-AC02-05CH11231. The work performed at UC Riverside was supported by the U.S. National Science Foundation under grant number CHE-1566636 (J.Z.).

## ■ REFERENCES

- (1) Marshall, W. M.; Deans, M. C. In *Recommended Figures of Merit for Green Monopropellants*, 49th AIAA/ASME/SAE/ASEE Joint Propulsion Conference, Session: Green Fuels I, AIAA, 2013; pp 2013–3722.
- (2) Leal, J. P.; Esperança, J. M. S. S.; Minas da Piedade, M. E.; Canongia Lopes, J. N.; Rebelo, L. P. N.; Seddon, K. R. The Nature of Ionic Liquids in the Gas Phase. *J. Phys. Chem. A* **2007**, *111*, 6176–6182.
- (3) Tsay, M.; Lafko, D.; Zwahlen, J.; Costa, W. In *Development of Busek 0.5N Green Monopropellant Thruster*, Proceedings of the Small Satellite Conference, Technical Session VII: Propulsion, SSC13-VII-7, 2013.
- (4) Sabard, J.; Catoire, L.; Chambreau, S. D.; Vaghjiani, G. L. Method for Predicting Hypergolic Mixture Flammability Limits: Application for Non-Ionic Liquid Based Systems. *Combust. Flame* **2017**, *176*, 547–553.
- (5) Savrun, E.; Sawhill, S. J. High Temperature Catalysts for Decomposition of Liquid Monopropellants and Methods for Producing the Same. U 9,149,795B2, Oct 06, 2015.
- (6) Chambreau, S. D.; Popolan-Vaida, D. M.; Vaghjiani, G. L.; Leone, S. R. Catalytic Decomposition of Hydroxylammonium Nitrate Ionic Liquid: Enhancement of NO Formation. *J. Phys. Chem. Lett.* **2017**, *8*, 2126–2130.
- (7) Chambreau, S. D.; Koh, C. J.; Popolan-Vaida, D. M.; Gallegos, C. J.; Hooper, J. B.; Bedrov, D.; Vaghjiani, G. L.; Leone, S. R. Flow-Tube Investigations of Hypergolic Reactions of a Dicyanamide Ionic Liquid Via Tunable Vacuum Ultraviolet Aerosol Mass Spectrometry. *J. Phys. Chem. A* **2016**, *120*, 8011–8023.
- (8) Chambreau, S. D.; Schenk, A. C.; Sheppard, A. J.; Yandek, G. R.; Vaghjiani, G. L.; Maciejewski, J.; Koh, C. J.; Golan, A.; Leone, S. R. Thermal Decomposition Mechanisms of Alkylimidazolium Ionic Liquids with Cyano-Functionalized Anions. *J. Phys. Chem. A* **2014**, *118*, 11119–11132.
- (9) Catoire, L.; Chambreau, S. D.; Vaghjiani, G. L. Chemical Kinetics Interpretation of Hypergolicity of Dicyanamide Ionic Liquid-Based Systems. *Combust. Flame* **2012**, *159*, 1759–1768.
- (10) Schneider, S.; Hawkins, T.; Rosander, M.; Vaghjiani, G.; Chambreau, S.; Drake, G. Ionic Liquids as Hypergolic Fuels. *Energy Fuels* **2008**, *22*, 2871–2872.
- (11) Chambreau, S. D.; Schneider, S.; Rosander, M.; Hawkins, T.; Gallegos, C. J.; Pastewait, M. F.; Vaghjiani, G. L. Fourier Transform Infrared Studies in Hypergolic Ignition of Ionic Liquids. *J. Phys. Chem. A* **2008**, *112*, 7816–7824.
- (12) Deetlefs, M.; Seddon, K. R.; Shara, M. Predicting Physical Properties of Ionic Liquids. *Phys. Chem. Chem. Phys.* **2006**, *8*, 642–649.
- (13) Izgorodina, E. I.; Seeger, Z. L.; Scarborough, D. L. A.; Tan, S. Y. S. Quantum Chemical Methods for the Prediction of Energetic, Physical, and Spectroscopic Properties of Ionic Liquids. *Chem. Rev.* **2017**, *117*, 6696–6754.
- (14) Zhou, Z.; Lee, J. K.; Kim, S. C.; Zare, R. N. Nanotip Ambient Ionization Mass Spectrometry. *Anal. Chem.* **2016**, *88*, 5542–5548.
- (15) Lee, J. K.; Jansson, E. T.; Nam, H. G.; Zare, R. N. High-Resolution Live-Cell Imaging and Analysis by Laser Desorption/

- Ionization Droplet Delivery Mass Spectrometry. *Anal. Chem.* **2016**, *88*, 5453–5461.
- (16) Lu, X.; Francis, S.; Motta, D.; Dimitratos, N.; Roldan, A. Mechanistic study of hydrazine decomposition on Ir(111). *Phys. Chem. Chem. Phys.* **2020**, *22*, 3883–3896.
- (17) Zhang, P.-X.; Wang, Y.-G.; Huang, Y.-Q.; Zhang, T.; Wu, G.-S.; Li, J. Density functional theory investigations on the catalytic mechanisms of hydrazine decompositions on Ir(111). *Catal. Today* **2011**, *165*, 80–88.
- (18) Konnov, A. A.; De Ruyck, J. Kinetic modeling of the decomposition and flames of hydrazine. *Combust. Flame* **2001**, *124*, 106–126.
- (19) Zhang, L.; van Duin, A. C. T.; Zybin, S. V.; Goddard, W. A., III Thermal Decomposition of Hydrazines from Reactive Dynamics Using the ReaxFF Reactive Force Field. *J. Phys. Chem. B* **2009**, *113*, 10770–10778.
- (20) Esparza, A. A.; Chambreau, S. D.; Vaghjiani, G. L.; Shafirovich, E. Two-Stage Decomposition of 2-Hydroxyethylhydrazinium Nitrate (HEHN). *Combust. Flame* **2020**, *220*, 1–6.
- (21) Schmidt, M. W.; Gordon, M. S. The Decomposition of Hydrazine in the Gas Phase and over an Iridium Catalyst. *Z. Phys. Chem.* **2013**, *227*, 1301.
- (22) Chowdhury, A.; Thynell, S. T. Kinetics of Decomposition of Energetic Ionic Liquids. *Propellants, Explos., Pyrotech.* **2010**, *35*, 572–581.
- (23) Kohn, D. W.; Clauberg, H.; Chen, P. Flash Pyrolysis Nozzle for Generation of Radicals in a Supersonic Jet Expansion. *Rev. Sci. Instrum.* **1992**, *63*, 4003–4005.
- (24) Chambreau, S. D.; Zhang, J.; Traeger, J. C.; Morton, T. H. Photoionization of Methyl t-Butyl Ether (MTBE) and t-Octyl Methyl Ether (TOME) and Analysis of their Pyrolyses by Supersonic Jet/Photoionization Mass Spectrometry. *Int. J. Mass Spectrom.* **2000**, *199*, 17–27.
- (25) Chambreau, S. D.; Zhang, J. VUV Photoionization Time-of-Flight Mass Spectrometry of Flash Pyrolysis of Silane and Disilane. *Chem. Phys. Lett.* **2001**, *343*, 482–488.
- (26) Chambreau, S. D.; Zhang, J. GeH<sub>x</sub> (x=0–3) and GenH<sub>x</sub> (n=2–7) in Flash Pyrolysis of GeH<sub>4</sub>. *Chem. Phys. Lett.* **2002**, *351*, 171–177.
- (27) Chambreau, S. D.; Lemieux, J.; Wang, L.; Zhang, J. Mechanistic Studies of the Pyrolysis of 1,3-Butadiene, 1,3-Butadiene-1,1,4,4-d<sub>4</sub>, 1,2-Butadiene, and 2-Butyne by Supersonic Jet/Photoionization Mass Spectrometry. *J. Phys. Chem. A* **2005**, *109*, 2190–2196.
- (28) Chambreau, S. D.; Boatz, J. A.; Vaghjiani, G. L.; Koh, C.; Kostko, O.; Golan, A.; Leone, S. R. Thermal Decomposition of 1-Ethyl-3-methylimidazolium Bromide Ionic Liquid. *J. Phys. Chem. A* **2012**, *116*, 5867–5876.
- (29) Chambreau, S. D.; Vaghjiani, G. L.; To, A.; Koh, C.; Strasser, D.; Kostko, O.; Leone, S. R. Heats of Vaporization of Room Temperature Ionic Liquids by Tunable Vacuum Ultraviolet Photoionization. *J. Phys. Chem. B* **2010**, *114*, 1361–1367.
- (30) Koh, C.; Liu, C.-L.; Harmon, C.; Strasser, D.; Golan, A.; Kostko, O.; Chambreau, S. D.; Vaghjiani, G. L.; Leone, S. R. Soft Ionization of Thermally Evaporated Hypersonic Ionic Liquid Aerosols. *J. Phys. Chem. A* **2011**, *115*, 4630–4635.
- (31) Strasser, D.; Goulay, F.; Belau, L.; Kostko, O.; Koh, C.; Chambreau, S. D.; Vaghjiani, G. L.; Ahmed, M.; Leone, S. R. Tunable Wavelength Soft Photoionization of Ionic Liquid Vapors. *J. Phys. Chem. A* **2010**, *114*, 879–883.
- (32) Strasser, D.; Goulay, F.; Kelkar, M. S.; Maginn, E. J.; Leone, S. R. Photoelectron Spectrum of Isolated Ion-Pairs in Ionic Liquid Vapor. *J. Phys. Chem. A* **2007**, *111*, 3191–3915.
- (33) Chambreau, S. D.; Vaghjiani, G. L.; Koh, C.; Golan, A.; Leone, S. R. Ultraviolet Photoionization Efficiency of the Vaporized Ionic Liquid 1-Butyl-3-methylimidazolium Tricyanomethanide: Direct Detection of the Intact Ion Pair. *J. Phys. Chem. Lett.* **2012**, *3*, 2910–2914.
- (34) Vékey, K. Internal Energy Effects in Mass Spectrometry. *J. Mass Spectrom.* **1996**, *31*, 445–463.
- (35) Gloaguen, E.; Mysak, E. R.; Leone, S. R.; Ahmed, M.; Wilson, K. R. Investigating the Chemical Composition of Mixed Organic-Inorganic Particles by “Soft” Vacuum Ultraviolet Photoionization: The Reaction of Ozone with Anthracene on Sodium Chloride Particles. *Int. J. Mass Spectrom.* **2006**, *258*, 74–85.
- (36) Liu, P.; Ziemann, P. J.; Kittelson, D. B.; McMurry, P. H. Generating Particle Beams of Controlled Dimensions and Divergence: I. Theory of Particle Motion in Aerodynamic Lenses and Nozzle Expansions. *Aerosol Sci. Technol.* **1995**, *22*, 293–311.
- (37) Friderichsen, A. V.; Radziszewski, J. G.; Nimlos, M. R.; Winter, P. R.; Dayton, D. C.; David, D. E.; Ellison, G. B. The Infrared Spectrum of the Matrix-Isolated Phenyl Radical. *J. Am. Chem. Soc.* **2001**, *123*, 1977–1988.
- (38) Belau, L.; Wilson, K. R.; Leone, S. R.; Ahmed, M. Vacuum Ultraviolet (VUV) Photoionization of Small Water Clusters. *J. Phys. Chem. A* **2007**, *111*, 10075–10083.
- (39) Wilson, K. R.; Jimenez-Cruz, M.; Nicolas, C.; Belau, L.; Leone, S. R.; Ahmed, M. Thermal Vaporization of Biological Nanoparticles: Fragment-Free Vacuum Ultraviolet Photoionization Mass Spectra of Tryptophan, Phenylalanine-Glycine-Glycine, and  $\beta$ -Carotene. *J. Phys. Chem. A* **2006**, *110*, 2106–2113.
- (40) Zhao, Y.; Truhlar, D. G. The M06 Suite of Density Functionals for Main Group Thermochemistry, Thermochemical kinetics, Non-covalent Interactions, Excited States, and Transition Elements: Two New Functionals and Systematic Testing of Four M06-class Functionals and 12 Other Functionals. *Theor. Chem. Acc.* **2008**, *120*, 215–241.
- (41) Frisch, M. J.; Trucks, G. W.; Schlegel, H. B.; Scuseria, G. E.; Robb, M. A.; Cheeseman, J. R.; Scalmani, G.; Barone, V.; Petersson, G. A.; Nakatsuji, H. et al. *Gaussian 16*, revision C.01; Gaussian Inc.: Wallingford, CT, 2016.
- (42) Howard, J. C.; Gever, G.; Neill, A. B.; Wei, P. H. L. The Thermal Decomposition of 2-Hydrazinoethanol and 1-Hydrazino-2-propanol. *J. Org. Chem.* **1961**, *26*, 1082–1083.
- (43) Ando, T.; Fujimoto, Y.; Morisaki, S. Analysis of Differential Scanning Calorimetric Data for Reactive Chemicals. *J. Hazard. Mater.* **1991**, *28*, 251–280.
- (44) Burgers, P. C.; Drewello, T.; Schwarz, H.; Terlouw, J. K. CH<sub>5</sub>N<sub>2</sub> Hydrazyl Radicals, Cations and Dication Radicals Studied by Mass Spectrometry. Is the N-protonated Formaldehyde Hydrason Cation +CH<sub>2</sub>-NH-NH<sub>2</sub> a Bridged Species? *Int. J. Mass Spectrom. Ion Processes* **1989**, *95*, 157–169.
- (45) Stein, S. E. Mass Spectra. In *NIST Chemistry WebBook*; Linstrom, P. J.; Mallard, W. G., Eds.; National Institute of Standards and Technology: Gaithersburg, MD, 2014.
- (46) Holzmeier, F.; Lang, M.; Fischer, I.; Hemberger, P.; Garcia, G. A.; Tang, X.; Loison, J. C. Assignment of High-Lying Bending Mode Levels in the Threshold Photoelectron Spectrum of NH<sub>2</sub>: a Comparison Between Pyrolysis and Fluorine-atom Abstraction Radical Sources. *Phys. Chem. Chem. Phys.* **2015**, *17*, 19507–19514.
- (47) Sun, H.; Law, C. K. Thermochemical and Kinetic Analysis of the Thermal Decomposition of Monomethylhydrazine: An Elementary Reaction Mechanism. *J. Phys. Chem. A* **2007**, *111*, 3748–3760.
- (48) Holzmeier, F.; Lang, M.; Hader, K.; Hemberger, P.; Fischer, I. H<sub>2</sub>CN<sup>+</sup> and H<sub>2</sub>CNH<sup>+</sup>: New Insight Into the Structure and Dynamics from Mass-Selected Threshold Photoelectron Spectra. *J. Chem. Phys.* **2013**, *138*, No. 214310.
- (49) Tarasenko, N. A.; Tishenkov, A. A.; Zaikin, V. G.; Volkova, V. V.; Gusel'nikov, L. E. Adiabatic Ionization Energy of Methylenimine. *Bull. Acad. Sci. USSR, Div. Chem. Sci.* **1986**, *35*, 2196.
- (50) Lias, S. G. Ionization Energy Evaluation. In *NIST Chemistry WebBook*; Linstrom, P. J.; Mallard, W. G., Eds.; National Institute of Standards and Technology: Gaithersburg, MD, 2005.
- (51) Hashemi, H.; Christensen, J. M.; Glarborg, P. High-pressure pyrolysis and oxidation of ethanol. *Fuel* **2018**, *218*, 247–257.
- (52) Li, J.; Kazakov, A.; Dryer, F. L. Ethanol Pyrolysis Experiments in a Variable Pressure Flow Reactor. *Int. J. Chem. Kinet.* **2001**, *33*, 859–867.

(53) Sivaramakrishnan, R.; Su, M. C.; Michael, J. V.; Klippenstein, S. J.; Harding, L. B.; Ruscic, B. Rate Constants for the Thermal Decomposition of Ethanol and Its Bimolecular Reactions with OH and D: Reflected Shock Tube and Theoretical Studies. *J. Phys. Chem. A* **2010**, *114*, 9425–9439.

(54) Park, J.; Zhu, R. S.; Lin, M. C. Thermal decomposition of ethanol. I. Ab Initio molecular orbital/Rice–Ramsperger–Kassel–Marcus prediction of rate constant and product branching ratios. *J. Chem. Phys.* **2002**, *117*, 3224–3231.

(55) Tao, W.; Klemm, R. B.; Nesbitt, F. L.; Stief, L. J. A Discharge Flow-Photoionization Mass Spectrometric Study of Hydroxymethyl Radicals (H<sub>2</sub>COH and H<sub>2</sub>COD): Photoionization Spectrum and Ionization Energy. *J. Phys. Chem. A* **1992**, *96*, 104–107.

(56) Bombach, R.; Stadelmann, J.-P.; Vogt, J. The Fragmentation and Isomerization of Internal Energy Selected Acetaldehyde Molecular Cations. *Chem. Phys.* **1981**, *60*, 293–299.

(57) Locht, R.; Leyh, B.; Denzer, W.; Hagenow, G.; Baumgärtel, H. The Photoionization of Ammonia Revisited. The Vibrational Autoionization of NH<sub>3</sub> and its Three Isotopomers in the 10–12 eV Photon Energy Range. *Chem. Phys.* **1991**, *155*, 407–422.

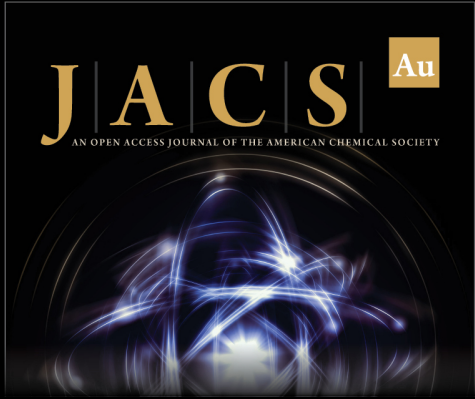
(58) Thomas, A. E.; Chambreau, S. D.; Redeker, N. D.; Esparza, A. A.; Shafirovich, E.; Ribbeck, T.; Sprenger, J. A. P.; Finze, M.; Vaghjani, G. L. Thermal Decomposition and Hypergolic Reaction of a Dicyanoborohydride Ionic Liquid. *J. Phys. Chem. A* **2020**, *124*, 864–874.

(59) Savee, J. D.; Soorkia, S.; Welz, O.; Selby, T. M.; Taatjes, C. A.; Osborn, D. L. Absolute Photoionization Cross-Section of the Propargyl Radical. *J. Chem. Phys.* **2012**, *136*, No. 134307.

(60) Zhang, T.; Tang, X. N.; Lau, K.-C.; Ng, C. Y.; Nicolas, C.; Peterka, D. S.; Ahmed, M.; Morton, M. L.; Ruscic, B.; Yang, R.; et al. Direct identification of propargyl radical in combustion flames by vacuum ultraviolet photoionization mass spectrometry. *J. Chem. Phys.* **2006**, *124*, No. 074302.

(61) Barbula, G. K.; Robbins, M. D.; Yoon, O. K.; Zuleta, I.; Zare, R. N. Desorption Electrospray Ionization: Achieving Rapid Sampling Rates. *Anal. Chem.* **2009**, *81*, 9035–9040.

(62) Badertscher, M.; Bischofberger, K.; Munk, M. E.; Pretsch, E. A Novel Formalism To Characterize the Degree of Unsaturation of Organic Molecules. *J. Chem. Inf. Comput. Sci.* **2001**, *41*, 889–893.



**JACS** Au  
AN OPEN ACCESS JOURNAL OF THE AMERICAN CHEMICAL SOCIETY

Editor-in-Chief  
**Prof. Christopher W. Jones**  
Georgia Institute of Technology, USA

**Open for Submissions** 

pubs.acs.org/jacsau  ACS Publications  
Most Trusted. Most Cited. Most Read.